Smart Structures and Systems, *Vol. 33, No. 5 (2024) 333-347*
https://doi.org/10.12989/sss.2024.33.5.333

Deflection aware smart structures by artificial intelligence algorithm

Qingyun Gao*[1], Yun Wang [1], Zhimin Zhou [1] and Khalid A. Alnowibet [2]

[1] *FAIR FRIEND Institute of Intelligent Manufacturing, Hangzhou Vocational & Technical College, Hangzhou 310018, China*
[2] *Statistics and Operations Research Department, College of Science, King Saud University, Riyadh, 11451, Saudi Arabia*

(*Received June 12, 2023, Revised May 2, 2024, Accepted May 11, 2024*)

Abstract. There has been an increasing interest in the construction of smart buildings that can actively monitor and react to their surroundings. The capacity of these intelligent structures to precisely predict and respond to deflection is a crucial feature that guarantees both their structural soundness and efficiency. Conventional techniques for determining deflection often depend on intricate mathematical models and computational simulations, which may be time- and resource-consuming. Artificial intelligence (AI) algorithms have become a potent tool for anticipating and controlling deflection in intelligent structures in response to these difficulties. The term "deflection-aware smart structures" in this sense refers to constructions that have AI algorithms installed that continually monitor and analyses deflection data in order to proactively detect any problems and take appropriate action. These structures anticipate deflection across a range of operating circumstances and environmental factors by using cutting-edge AI approaches including deep learning, reinforcement learning, and neural networks. AI systems are able to predict real-time deflection with high accuracy by using data from embedded sensors and actuators. This capability enables the systems to identify intricate patterns and linkages. Intelligent buildings have the potential to self-correct in order to reduce deflection and maximize performance. In conclusion, the development of deflection-aware smart structures is a major stride forward for structural engineering and has enormous potential to enhance the performance, safety, and dependability of designed systems in a variety of industries.

Keywords: applied voltage; artificial intelligence algorithm; DQA; HDQM; piezoelectric materials

1. Introduction

A smart city refers to an urban environment that harnesses cutting-edge technology and data analytic methodologies to enhance the quality of life of its residents (Wang and Zhou 2023), maximize resource consumption (Shafiullah *et al*. 2023), and promote sustainability (Chen 2023). This topic has attracted increased attention in the past few decades, as cities throughout the globe confront different difficulties such as traffic congestion (Guo *et al*. 2020), contamination of the environment (Chu *et al*. 2021), and aging infrastructure. Smart city efforts attempt to solve these difficulties via the inclusion of technical breakthroughs like the Internet of Things (IoT) (Bhardwaj *et al*. 2022), intelligent machines (AI) (Herath and Mittal 2022), and big data analytics (Khan 2022) to enhance municipal operations and services.

Bibri and Krogstie (2017a) define a smart city as a city that utilizes technology to improve its livability, workability, and sustainability. Furthermore, they contend that a smart city should be tailored to the requirements and desires of its inhabitants, rather than exclusively prioritizing technological remedies. Additional research has examined specific aspects of smart cities, such as the application of Internet of Things (IoT) technology in transportation (Krishankumar and Ecer 2023), the challenges associated with implementing smart city projects in developing nations (Al Nuaimi *et al*. 2015), and the role of citizen involvement in smart city initiatives (Vahidnia 2022). In addition to these studies, there have also been other case studies of smart city efforts across the globe. Caragliu *et al*. (2013) investigate the smart city strategies of various European cities, while Bibri and Krogstie (2017b) explore the execution of smart city projects in Singapore. The case studies provide valuable insights into the difficulties and possibilities of implementing smart city programs in various settings (Quan and Solheim 2023).

Piezoelectricity is the term used to describe the behavior of some materials that generate an electric charge when exposed to mechanical stress (Cao and AlKubaisy 2022, Chen *et al*. 2022, Jangid 2022, Zhong *et al*. 2022, Chase *et al*. 2023). The distinctive characteristic of piezoelectric materials has rendered them a crucial element in the development of smart cities. Piezoelectric materials in smart cities provide several advantages, such as capturing energy, monitoring and actuator (Rani and Kumar 2022), and inspection of structural health (Mishra *et al*. 2022). Piezoelectric materials have a significant influence on the monitoring of building health in smart cities. Piezoelectric sensors have the ability to detect changes in physical stress or pressure and transform them into electrical signals. This characteristic makes them valuable for examining the structural integrity of buildings and other forms of infrastructure (He *et al*. 2022). Engineers may monitor the building's reaction to external variables like wind,

*Corresponding author, Ph.D.,
E-mail: gaoqingyun358@hotmail.com

ISSN: 1738-1584 (Print), 1738-1991 (Online)

earthquakes, or high loads by incorporating piezoelectric sensors within the structure (Gordan *et al*. 2022). Subsequently, this data may be used to forecast the future performance of the structure and detect any possible harm or structural vulnerabilities (Shetty *et al*. 2023). Furthermore, piezoelectric actuators have the capability to exert precise mechanical stress or pressure, allowing for effective management of any damage or instability (Feng and Liang 2022). In summary, including piezoelectric materials in the construction of buildings for health monitoring purposes may contribute to the durability and security of structures in smart cities (Ju *et al*. 2023).

Anisotropic materials have unique properties that change with orientation in relation to their internal structure or external loading conditions, in contrast to isotropic materials, which have uniform properties regardless of direction (Zhang *et al*. 2022, She *et al*. 2023). They are useful and adaptable for a variety of technical applications where directional dependency is crucial because of their special quality (He *et al*. 2024, Wang *et al*. 2024). Anisotropic materials occur naturally and in a variety of artificial forms, such as sophisticated synthetic materials, biological tissues, composites, and crystals (Zhang *et al*. 2016, Luo *et al*. 2023). The asymmetrical arrangement of atoms, molecules, or microstructures within the material is the cause of their anisotropic behaviour, which results in directional variations in mechanical stiffness, optical properties, thermal conductivity, electrical conductivity, and other material properties (Guo and Zhang 2023, Zhou *et al*. 2024).

Single crystals are one of the most prevalent types of anisotropic materials; their ordered atomic arrangement causes them to display distinct mechanical characteristics along various crystallographic axes (Zhu *et al*. 2017, Mi *et al*. 2023). Sophisticated methods for precisely simulating complex systems include agent-based modelling, computational fluid dynamics (CFD), and finite element analysis (FEA) (Liu *et al*. 2020, Yang *et al*. 2023a). Stochastic models addressing uncertainty in systems like financial markets or risk analysis (Yang *et al*. 2022, 2023b), individual agents with specific behaviours like traffic flow (Taheri *et al*. 2020, Feng *et al*. 2021), or social dynamics, discrete processes like industrial workflows or queuing systems (Liu *et al*. 2021, Taheri *et al*. 2021), and continuous systems with changing variables over time can all be modelled by computer simulations.

Additionally, computer simulations play a critical role in performance enhancement, issue identification (Firouzianhaji *et al*. 2021, Mehrabi *et al*. 2021a), and structural, mechanical, and electrical system design optimisation (Chen *et al*. 2023, Song *et al*. 2024). Simulations have the potential to improve patient outcomes and healthcare delivery by forecasting the course of diseases, streamlining medical procedures, and assessing the efficacy of therapies (Hu *et al*. 2023, Wu *et al*. 2023). To sum up, computer simulation is a vital tool for decision-making across a range of domains, promoting technological innovation and scientific research (Toghroli *et al*. 2020, Han *et al*. 2023 a, b). Through the provision of insights into system behaviours under various settings, simulations facilitate novel idea exploration, practical problem solving, and knowledge advancement in their respective domains.

Artificial intelligence relies heavily on machine learning, which enables computers to autonomously identify patterns in datasets without explicit programming. This feature is applicable to a wide range of subjects, including but not limited to statistics, demonstrating its broad application across several domains (Qiu 2019, Qiu and Wang 2024). The results of earlier studies may be used as the starting point for Refs. (Taheri *et al*. 2019, Mehrabi *et al*. 2021b). The development of co-culture systems with the goal of increasing the productivity and efficiency of biomass transformation has advanced significantly in recent years, according to studies. The co-culture system incorporating Clostridium aceticum and Clostridium cellulovorans was established by Xia *et al*. (2017), demonstrating the synergistic interactions between these bacteria that resulted in better biomass transformation capacities. Comparably, Horne *et al*. (2020) investigated the potential of coffee and theophylline to alter gene expression and enzyme activity, hence influencing cellular processes, by studying their inhibitory effects on β-galactosidase activity and expression in Escherichia coli. Moreover, Mock *et al*. (2021) studied enzyme activity and substrate promiscuity in a variety of microbial cultures. Their investigation of the enzyme complex's substrate promiscuity, which was reported in Biotechnology Notes, provided insight into its capacity to catalyse a variety of substrates. Furthermore, Mock *et al*. (2024) investigated the biodegradation of theophylline by an optimised Escherichia coli strain, leading to the generation of 1-methylxanthine, in their study published in the Journal of Biotechnology.

While the development of smart cities heavily relies on piezoelectricity, no study to date has examined the structural health monitoring of smart walls via an assessment of their inherent frequency. By using piezoelectricity, this study adopts a novel strategy to increase public awareness of the potentially dangerous characteristics of structures. Reciprocally, electrical power and displacement may be converted into one another via piezoelectric materials. In this work, a critical threshold for the displacements is established using this feature. The case study of a rectangular wall with a single free edge at the top, or GPLR-FGP, is the main subject of this study. Gradually increasing the voltage will occur until the natural frequency gets close to zero. The wall's stability is directly threatened by this circumstance. Consequently, the wall displacements under these conditions might be considered the system's critical deflections. The wall's controlling equations are established in relation to HOSDT. DQA is used to ascertain the wall's inherent frequency. By training a deep neural network with the examples obtained from the designated numerical approach, deep learning is used to accelerate the computing process.

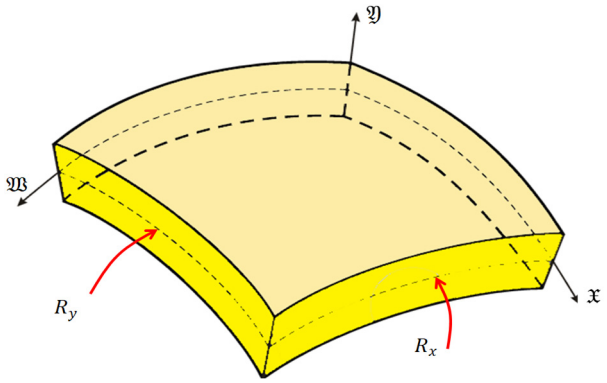

Fig. 1 Diagram depicting the schematic of the GPLR-FGP wall

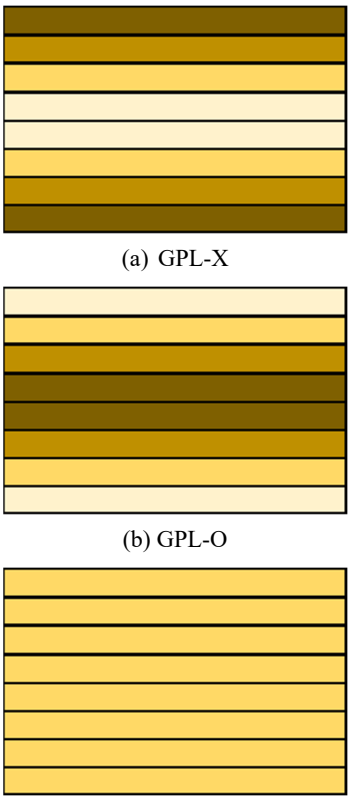

(a) GPL-X

(b) GPL-O

(c) GPL-UD

Fig. 2 Three dispersion patterns of GPL that occur across the transverse of the GPLR-FGP wall

2. Formulation

2.1 Schematics of the case study

Fig. 1 illustrates the schematic representation of the GPLR-FGP wall, where b represents its width, a represents its length, and h represents its thickness.

Fig. 2 illustrates the dispersion patterns of the GPL along the wall's thickness.

2.2 Effective material properties

This study assumes that the wall consists of N_L layers of the GPL reinforced piezoelectric plate with a PVDF matrix. The mechanical characteristics of PVDF and GPL are shown in Table 1.

Table 1 Mechanical properties of PVDF (Wang and Liew 2003) and GPL (Song *et al*. 2017)

GPL	$E_G = 1.01$ TPa	$\nu_G = 0.186$	$\rho_G = 1920\ \mathrm{kg/m^3}$
PVDF	$E_M = 1.44$ GPa	$\nu_M = 0.29$	$\rho_M = 800\ \mathrm{kg/m^3}$

Table 2 Dielectric and piezoelectric constants of PVDF (Mitchell and Reddy 1995)

$e_{31,M}$	$e_{32,M}$	$e_{33,M}$	$e_{24,M}$	$e_{15,M}$
32.075×10^{-3}	-4.07×10^{-3}	-21.19×10^{-3}	-12.65×10^{-3}	-15.93×10^{-3}
$\mu_{11,M}$	$\mu_{22,M}$	$\mu_{33,M}$		
53.985×10^{-12}	66.375×10^{-12}	59.295×10^{-12}		

Units: $e_{ij,M}\left(\frac{C}{M^2}\right)$, $\mu_{ij,M}\left(\frac{F}{m}\right)$

Furthermore, the dielectric and piezoelectric constants of PVDF may be found in Table 2 (Mitchell and Reddy 1995).

With the aid of Ref. (Mao and Zhang 2018), the dispersion patterns of GPL are defined as below

Pattern U

$$f_i = \Lambda_{GPL}, \tag{1}$$

Pattern X

$$\begin{aligned} f_i &= \left(\frac{N}{2} + 1 - i\right) f^* \quad \text{if} \quad i \le \frac{N}{2} \\ f_i &= \left(i - \frac{N}{2}\right) f^* \quad \text{if} \quad i > \frac{N}{2} \end{aligned}, \tag{2}$$

Pattern O

$$\begin{aligned} f_i &= i f^* \quad \text{if} \quad i \le \frac{N}{2} \\ f_i &= (N + 1 - i) f^* \quad \text{if} \quad i > \frac{N'}{2} \end{aligned} \tag{3}$$

Where

$$f^* = \frac{2}{1 + \frac{N}{2}} \Lambda_{GPL}. \tag{4}$$

Here, f_i $(i = 1,2,\ldots,N_L)$, f^* and Λ_{GPL} represent the volume fraction of GPL at the ith layer, the average volume fraction of GPL, and the overall volume fraction of GPL, respectively. Furthermore, the PVDF matrix is believed to be tightly linked with GPL nanoparticles. The micromechanics model proposed by Halpin-Tsai provides a more precise prediction of the elastic moduli of GPL/polymer composites compared to the micromechanics model of Mori-Tanaka. The Halpin-Tsai parallel model properly calculates the Young's modulus of the GPLR-PVDF composites when Λ_{GPL} is less than 1%. The dielectric and piezoelectric properties of the dielectric and

GPL are β times greater than those of PVDF, and the piezoelectric multiple is represented by ξ. Consequently, the layer-dependent elastic modulus of the piezoelectric composite plate may be obtained as

$$E_{Ci} = \frac{1 + \frac{2l_{GPL}}{3t_{GPL}}\eta_L f_i}{1 - \eta_L f_i} E_M. \tag{5}$$

where

$$\eta_L = \frac{\frac{E_G}{E_M} - 1}{\frac{E_G}{E_M} + \frac{2l_{GPL}}{3t_{GPL}}}. \tag{6}$$

here, E_M, E_G and E_{Ci} represent in order the elastic modulus of the matrix, GPL, and the composite material. Length and thickness of the GPL nanoplates are denoted by l_{GPL} and t_{GPL}. Furthermore, the well-recognized principle of mixes is used to articulate other characteristics of the composite wall as shown below.

$$\begin{aligned} \rho_i &= \rho_G f_i + \rho_M(1 - f_i) \\ \nu_i &= \nu_G f_i + \nu_M(1 - f_i) \\ e_i &= e_G f_i + e_M(1 - f_i) \\ \mu_i &= \mu_G f_i + \mu_M(1 - f_i) \end{aligned}. \tag{7}$$

The i[th] layer of the composite is characterized by its effective mass density (ρ_i), Poisson's ratio (ν_i), dielectric constant (μ_i), and piezoelectric constant (e_i). The subscripts M and G in Eq. (7) represent the matrix and GPL, respectively.

2.3 Displacement fields

The displacement field based on the HOSDT is written as

$$\begin{aligned} \mathcal{U}(\mathfrak{W},\mathfrak{X},\mathfrak{Y},t) &= \mathcal{U}_0(\mathfrak{W},\mathfrak{X},t) + \mathfrak{Y}\mathcal{U}_1(\mathfrak{W},\mathfrak{X},t) \\ &\quad + \mathfrak{Y}^2\mathcal{U}_2(\mathfrak{W},\mathfrak{X},t) + \mathfrak{Y}^3\mathcal{U}_3(\mathfrak{W},\mathfrak{X},t) \\ &\quad + \mathfrak{Y}^4\mathcal{U}_4(\mathfrak{W},\mathfrak{X},t) + \mathfrak{Y}^5\mathcal{U}_5(\mathfrak{W},\mathfrak{X},t), \\ \mathcal{V}(\mathfrak{W},\mathfrak{X},\mathfrak{Y},t) &= \mathcal{V}_0(\mathfrak{W},\mathfrak{X},t) + \mathfrak{Y}\mathcal{V}_1(\mathfrak{W},\mathfrak{X},t) \\ &\quad + \mathfrak{Y}^2\mathcal{V}_2(\mathfrak{W},\mathfrak{X},t) + \mathfrak{Y}^3\mathcal{V}_3(\mathfrak{W},\mathfrak{X},t) \\ &\quad + \mathfrak{Y}^4\mathcal{V}_4(\mathfrak{W},\mathfrak{X},t) + \mathfrak{Y}^5\mathcal{V}_5(\mathfrak{W},\mathfrak{X},t), \\ \mathcal{W}(\mathfrak{W},\mathfrak{X},\mathfrak{Y},t) &= \mathcal{W}_0(\mathfrak{W},\mathfrak{X},t) + \mathfrak{Y}\mathcal{W}_1(\mathfrak{W},\mathfrak{X},t) \\ &\quad + \mathfrak{Y}^2\mathcal{W}_2(\mathfrak{W},\mathfrak{X},t) + \mathfrak{Y}^3\mathcal{W}_3(\mathfrak{W},\mathfrak{X},t) \\ &\quad + \mathfrak{Y}^4\mathcal{W}_4(\mathfrak{W},\mathfrak{X},t) + \mathfrak{Y}^5\mathcal{W}_5(\mathfrak{W},\mathfrak{X},t). \end{aligned} \tag{8}$$

2.4 Compatibility conditions

Eq. (9) presents the stress-strain relations specified for FGP materials

$$\begin{aligned} \sigma_{\mathfrak{W}\mathfrak{W}} &= \mathbb{f}_{11}\varepsilon_{\mathfrak{W}\mathfrak{W}} + \mathbb{f}_{12}\varepsilon_{\mathfrak{X}\mathfrak{X}} + \mathbb{f}_{13}\varepsilon_{\mathfrak{Y}\mathfrak{Y}} + e_{31}\frac{\partial \emptyset}{\partial \mathfrak{W}}, \\ \sigma_{\mathfrak{X}\mathfrak{X}} &= \mathbb{f}_{12}\varepsilon_{\mathfrak{W}\mathfrak{W}} + \mathbb{f}_{22}\varepsilon_{\mathfrak{X}\mathfrak{X}} + \mathbb{f}_{23}\varepsilon_{\mathfrak{Y}\mathfrak{Y}} + e_{32}\frac{\partial \emptyset}{\partial \mathfrak{X}}, \\ \sigma_{\mathfrak{Y}\mathfrak{Y}} &= \mathbb{f}_{13}\varepsilon_{\mathfrak{W}\mathfrak{W}} + \mathbb{f}_{23}\varepsilon_{\mathfrak{X}\mathfrak{X}} + \mathbb{f}_{33}\varepsilon_{\mathfrak{Y}\mathfrak{Y}} + e_{33}\frac{\partial \emptyset}{\partial \mathfrak{Y}}, \\ \tau_{\mathfrak{X}\mathfrak{Y}} &= \mathbb{f}_{44}\gamma_{\mathfrak{X}\mathfrak{Y}} + e_{24}\frac{\partial \emptyset}{\partial \mathfrak{X}}, \\ \tau_{\mathfrak{W}\mathfrak{Y}} &= \mathbb{f}_{55}\gamma_{\mathfrak{W}\mathfrak{Y}} + e_{15}\frac{\partial \emptyset}{\partial \mathfrak{W}}, \\ \tau_{\mathfrak{W}\mathfrak{X}} &= \mathbb{f}_{66}\gamma_{\mathfrak{W}\mathfrak{X}}, \end{aligned} \tag{9}$$

Moreover

$$\begin{aligned} \mathrm{D_x} &= \mathrm{e_{15}}\gamma_{\mathrm{xz}} - \eta_{11}\frac{\partial \emptyset}{\partial \mathrm{x}}, \\ \mathrm{D_y} &= \mathrm{e_{15}}\gamma_{\mathrm{yz}} - \eta_{22}\frac{\partial \emptyset}{\partial \mathrm{y}}, \\ \mathrm{D_z} &= \mathrm{e_{31}}\varepsilon_{\mathrm{xx}} + \mathrm{e_{32}}\varepsilon_{\mathrm{yy}} - \eta_{33}\frac{\partial \emptyset}{\partial \mathrm{z}}, \end{aligned} \tag{10}$$

The variables $\mathbb{f}_{ij}$, η_{ii}, and e_{ij} represent the elasticity, dielectric, and piezoelectric constants, respectively. Furthermore, D_i and E_i represent the electric displacement and intensity of the electric field of the piezoelectric plate, respectively. Furthermore, Eq. (11) expresses the magnitudes of the electric and magnetic fields, denoted as $E_{\mathfrak{W}}$, $E_{\mathfrak{X}}$, and $E_{\mathfrak{Y}}$, in the following manner

$$E_{\mathfrak{W}} = -\frac{\partial \varphi}{\partial \mathfrak{W}}, \quad E_{\mathfrak{X}} = -\frac{\partial \varphi}{\partial \mathfrak{X}}, \quad E_{\mathfrak{Y}} = -\frac{\partial \varphi}{\partial \mathfrak{Y}}, \tag{11}$$

The electric potential in Eq. (11) would be considered as follow

$$\begin{aligned} &\varphi(\mathfrak{W},\mathfrak{X},\mathfrak{Y},t) = -\cos(\beta\mathfrak{Y})\,\Phi(\mathfrak{W},\mathfrak{X},t) + \frac{2\mathfrak{Y}\Phi_o}{h}, \\ &\text{where } \beta = \frac{\pi}{h} \end{aligned} \tag{12}$$

Moreover, $\phi(\mathfrak{W},\mathfrak{X},t)$ denotes the spatial variation of the electric potential in the longitudinal and latitudinal orientations. Also, Φ_o in Eq. (12) represents the initial external electric potential. Following equation (Eq. (13)) articulates the terms of $\mathbb{f}_{ij}$ as

$$\begin{aligned} \mathbb{f}_{22} = \mathbb{f}_{33} = \mathbb{f}_{11} &= \frac{E(1-\nu)}{(1-2\nu)(1+\nu)}, \\ \mathbb{f}_{12} = \mathbb{f}_{13} = \mathbb{f}_{23} &= \frac{\nu E}{(1-2\nu)(1+\nu)}, \\ \mathbb{f}_{44} = \mathbb{f}_{55} = \mathbb{f}_{66} &= \frac{E}{2(1+\nu)}. \end{aligned} \tag{13}$$

Following equation (Eq. (14)) articulates the strains in terms of displacements as

$$\begin{aligned} &\varepsilon_{\mathfrak{W}\mathfrak{W}} = \frac{\partial \mathcal{U}}{\partial \mathfrak{W}} + \frac{\mathcal{W}}{R_x}, \quad \varepsilon_{\mathfrak{X}\mathfrak{X}} = \frac{\partial \mathcal{V}}{\partial \mathfrak{X}} + \frac{\mathcal{W}}{R_y}, \quad \varepsilon_{\mathfrak{Y}\mathfrak{Y}} = \frac{\partial \mathcal{W}}{\partial \mathfrak{Y}}, \\ &\gamma_{\mathfrak{W}\mathfrak{X}} = \frac{\partial \mathcal{U}}{\partial \mathfrak{X}} + \frac{\partial \mathcal{V}}{\partial \mathfrak{W}}, \quad \gamma_{\mathfrak{W}\mathfrak{Y}} = \frac{\partial \mathcal{U}}{\partial \mathfrak{Y}} + \frac{\partial \mathcal{W}}{\partial \mathfrak{W}} - \frac{\mathcal{U}}{R_x}, \\ &\gamma_{\mathfrak{X}\mathfrak{Y}} = \frac{\partial \mathcal{V}}{\partial \mathfrak{Y}} + \frac{\partial \mathcal{W}}{\partial \mathfrak{X}} - \frac{\mathcal{V}}{R_y}. \end{aligned} \tag{14}$$

2.5 Governing equations and Hamilton principle

Eq. (15) represents the Hamilton principle in the way of deriving the governing equations

$$\int_{t_1}^{t_2} \left(\delta\Pi_k - \delta\Pi_{e_1} - \delta\Pi_{e_2} - \left(\delta\Pi_{w_1} + \delta\Pi_{w_2}\right)\right) dt = 0, \tag{15}$$

The subsequent relations present the process of determining each individual term used in Eq. (15)

$$
\begin{aligned}
\Pi_k &= \frac{1}{2}\int\left[\rho\left\{\left(\frac{\partial \mathcal{U}}{\partial t}\right)^2+\left(\frac{\partial \mathcal{V}}{\partial t}\right)^2+\left(\frac{\partial \mathcal{W}}{\partial t}\right)^2\right\}\right]dV,\\
\Pi_{e_1} &= \frac{1}{2}\int\{\sigma_{\mathfrak{W}\mathfrak{W}}\varepsilon_{\mathfrak{W}\mathfrak{W}}+\sigma_{\mathfrak{x}\mathfrak{x}}\varepsilon_{\mathfrak{x}\mathfrak{x}}+\sigma_{\mathfrak{y}\mathfrak{y}}\varepsilon_{\mathfrak{y}\mathfrak{y}}+\tau_{\mathfrak{x}\mathfrak{y}}\gamma_{\mathfrak{x}\mathfrak{y}}\\
&\qquad +\tau_{\mathfrak{W}\mathfrak{y}}\gamma_{\mathfrak{W}\mathfrak{y}}+\tau_{\mathfrak{W}\mathfrak{x}}\gamma_{\mathfrak{W}\mathfrak{x}}\}dV.\\
\Pi_{e_2} &= -\int\{D_{\mathfrak{W}}E_{\mathfrak{W}}+D_{\mathfrak{x}}E_{\mathfrak{x}}+D_{\mathfrak{y}}E_{\mathfrak{y}}\}dV,\\
\Pi_{\mathcal{W}_1} &= \frac{1}{2}\int N_p\left(\left(\frac{\partial \mathcal{W}_0}{\partial \mathfrak{W}}\right)^2+\left(\frac{\partial \mathcal{W}_0}{\partial \mathfrak{x}}\right)^2\right)dA.\\
\Pi_{\mathcal{W}_2} &= \frac{1}{2}\int Psin(\Omega t)\mathcal{W}_0 dA.
\end{aligned}
\tag{16}
$$

where $N_p=-2(e_{31}-\frac{c_{13}e_{33}}{c_{33}})\Phi_0$.

Substituting Eqs. (16) into Eq. (15) brings about the following relations

$$
\begin{aligned}
\delta\mathcal{U}_0:\ & \frac{\partial \mathfrak{N}_{\mathfrak{W}\mathfrak{W}}}{\partial \mathfrak{W}}+\frac{\partial \mathfrak{N}_{\mathfrak{W}\mathfrak{x}}}{\partial \mathfrak{x}}+\frac{\mathfrak{N}_{\mathfrak{W}\mathfrak{y}}}{R_x}\\
&=I_0\frac{\partial^2\mathcal{U}_0}{\partial t^2}+I_1\frac{\partial^2\mathcal{U}_1}{\partial t^2}+I_2\frac{\partial^2\mathcal{U}_2}{\partial t^2}+I_3\frac{\partial^2\mathcal{U}_3}{\partial t^2}\\
&\quad +I_4\frac{\partial^2\mathcal{U}_4}{\partial t^2}+I_5\frac{\partial^2\mathcal{U}_5}{\partial t^2},\\
\delta\mathcal{V}_0:\ & \frac{\partial \mathfrak{N}_{\mathfrak{x}\mathfrak{x}}}{\partial \mathfrak{x}}+\frac{\partial \mathfrak{N}_{\mathfrak{W}\mathfrak{x}}}{\partial \mathfrak{W}}+\frac{\mathfrak{N}_{\mathfrak{x}\mathfrak{y}}}{R_y}\\
&=I_0\frac{\partial^2\mathcal{V}_0}{\partial t^2}+I_1\frac{\partial^2\mathcal{V}_1}{\partial t^2}+I_2\frac{\partial^2\mathcal{V}_2}{\partial t^2}+I_3\frac{\partial^2\mathcal{V}_3}{\partial t^2}\\
&\quad +I_4\frac{\partial^2\mathcal{V}_4}{\partial t^2}+I_5\frac{\partial^2\mathcal{V}_5}{\partial t^2},\\
\delta\mathcal{W}_0:\ & \frac{\partial \mathfrak{N}_{\mathfrak{W}\mathfrak{y}}}{\partial \mathfrak{W}}+\frac{\partial \mathfrak{N}_{\mathfrak{x}\mathfrak{y}}}{\partial \mathfrak{x}}-\frac{\mathfrak{N}_{\mathfrak{W}\mathfrak{W}}}{R_x}-\frac{\mathfrak{N}_{\mathfrak{x}\mathfrak{x}}}{R_y}\\
&\quad -\mathfrak{N}_p\left(\frac{\partial^2\mathcal{W}_0}{\partial \mathfrak{W}^2}+\frac{\partial^2\mathcal{W}_0}{\partial \mathfrak{x}^2}\right)+Psin(\Omega t)\\
&=I_0\frac{\partial^2\mathcal{W}_0}{\partial t^2}+I_1\frac{\partial^2\mathcal{W}_1}{\partial t^2}+I_2\frac{\partial^2\mathcal{W}_2}{\partial t^2}+I_3\frac{\partial^2\mathcal{W}_3}{\partial t^2}\\
&\quad +I_4\frac{\partial^2\mathcal{W}_4}{\partial t^2}+I_5\frac{\partial^2\mathcal{W}_5}{\partial t^2},\\
\delta\mathcal{U}_1:\ & \frac{\partial \mathfrak{M}_{\mathfrak{W}\mathfrak{W}}}{\partial \mathfrak{W}}+\frac{\partial \mathfrak{M}_{\mathfrak{W}\mathfrak{x}}}{\partial \mathfrak{x}}-\mathfrak{N}_{\mathfrak{W}\mathfrak{y}}+\frac{\mathfrak{M}_{\mathfrak{W}\mathfrak{y}}}{R_x}\\
&=I_1\frac{\partial^2\mathcal{U}_0}{\partial t^2}+I_2\frac{\partial^2\mathcal{U}_1}{\partial t^2}+I_3\frac{\partial^2\mathcal{U}_2}{\partial t^2}+I_4\frac{\partial^2\mathcal{U}_3}{\partial t^2}\\
&\quad +I_5\frac{\partial^2\mathcal{U}_4}{\partial t^2}+I_6\frac{\partial^2\mathcal{U}_5}{\partial t^2},\\
\delta\mathcal{V}_1:\ & \frac{\partial \mathfrak{M}_{\mathfrak{x}\mathfrak{x}}}{\partial \mathfrak{x}}+\frac{\partial \mathfrak{M}_{\mathfrak{W}\mathfrak{x}}}{\partial \mathfrak{W}}-\mathfrak{N}_{\mathfrak{x}\mathfrak{y}}+\frac{\mathfrak{M}_{\mathfrak{x}\mathfrak{y}}}{R_y}\\
&=I_1\frac{\partial^2\mathcal{V}_0}{\partial t^2}+I_2\frac{\partial^2\mathcal{V}_1}{\partial t^2}+I_3\frac{\partial^2\mathcal{V}_2}{\partial t^2}+I_4\frac{\partial^2\mathcal{V}_3}{\partial t^2}\\
&\quad +I_5\frac{\partial^2\mathcal{V}_4}{\partial t^2}+I_6\frac{\partial^2\mathcal{V}_5}{\partial t^2},\\
\delta\mathcal{W}_1:\ & \frac{\partial \mathfrak{M}_{\mathfrak{W}\mathfrak{y}}}{\partial \mathfrak{W}}+\frac{\partial \mathfrak{M}_{\mathfrak{x}\mathfrak{y}}}{\partial \mathfrak{x}}-\mathfrak{N}_{\mathfrak{y}\mathfrak{y}}-\frac{\mathfrak{M}_{\mathfrak{W}\mathfrak{W}}}{R_x}-\frac{\mathfrak{M}_{\mathfrak{x}\mathfrak{x}}}{R_y}\\
&=I_1\frac{\partial^2\mathcal{W}_0}{\partial t^2}+I_2\frac{\partial^2\mathcal{W}_1}{\partial t^2}+I_3\frac{\partial^2\mathcal{W}_2}{\partial t^2}+I_4\frac{\partial^2\mathcal{W}_3}{\partial t^2}\\
&\quad +I_5\frac{\partial^2\mathcal{W}_4}{\partial t^2}+I_6\frac{\partial^2\mathcal{W}_5}{\partial t^2},\\
\delta\mathcal{U}_2:\ & \frac{\partial \mathfrak{P}_{\mathfrak{W}\mathfrak{W}}}{\partial \mathfrak{W}}+\frac{\partial \mathfrak{P}_{\mathfrak{W}\mathfrak{x}}}{\partial \mathfrak{x}}-2\mathfrak{M}_{\mathfrak{W}\mathfrak{y}}+\frac{\mathfrak{P}_{\mathfrak{W}\mathfrak{y}}}{R_x}\\
&=I_2\frac{\partial^2\mathcal{U}_0}{\partial t^2}+I_3\frac{\partial^2\mathcal{U}_1}{\partial t^2}+I_4\frac{\partial^2\mathcal{U}_2}{\partial t^2}+I_5\frac{\partial^2\mathcal{U}_3}{\partial t^2}\\
&\quad +I_6\frac{\partial^2\mathcal{U}_4}{\partial t^2}+I_7\frac{\partial^2\mathcal{U}_5}{\partial t^2},\\
\delta\mathcal{V}_2:\ & \frac{\partial \mathfrak{P}_{\mathfrak{x}\mathfrak{x}}}{\partial \mathfrak{x}}+\frac{\partial \mathfrak{P}_{\mathfrak{W}\mathfrak{x}}}{\partial \mathfrak{W}}-2\mathfrak{M}_{\mathfrak{x}\mathfrak{y}c}+\frac{\mathfrak{P}_{\mathfrak{x}\mathfrak{y}}}{R_y}\\
&=I_2\frac{\partial^2\mathcal{V}_0}{\partial t^2}+I_3\frac{\partial^2\mathcal{V}_1}{\partial t^2}+I_4\frac{\partial^2\mathcal{V}_2}{\partial t^2}+I_5\frac{\partial^2\mathcal{V}_3}{\partial t^2}\\
&\quad +I_6\frac{\partial^2\mathcal{V}_4}{\partial t^2}+I_7\frac{\partial^2\mathcal{V}_5}{\partial t^2},\\
\delta\mathcal{W}_2:\ & \frac{\partial \mathfrak{P}_{\mathfrak{W}\mathfrak{y}}}{\partial \mathfrak{W}}+\frac{\partial \mathfrak{P}_{\mathfrak{x}\mathfrak{y}}}{\partial \mathfrak{x}}-2\mathfrak{M}_{\mathfrak{y}\mathfrak{y}}-\frac{\mathfrak{P}_{\mathfrak{W}\mathfrak{W}}}{R_x}-\frac{\mathfrak{P}_{\mathfrak{x}\mathfrak{x}}}{R_y}\\
&=I_2\frac{\partial^2\mathcal{W}_0}{\partial t^2}+I_3\frac{\partial^2\mathcal{W}_1}{\partial t^2}+I_4\frac{\partial^2\mathcal{W}_2}{\partial t^2}+I_5\frac{\partial^2\mathcal{W}_3}{\partial t^2}\\
&\quad +I_6\frac{\partial^2\mathcal{W}_4}{\partial t^2}+I_7\frac{\partial^2\mathcal{W}_5}{\partial t^2},\\
\delta\mathcal{U}_3:\ & \frac{\partial \mathfrak{f}_{\mathfrak{W}\mathfrak{W}}}{\partial \mathfrak{W}}+\frac{\partial \mathfrak{f}_{\mathfrak{W}\mathfrak{x}}}{\partial \mathfrak{x}}-3\mathfrak{P}_{\mathfrak{W}\mathfrak{y}}+\frac{\mathfrak{f}_{\mathfrak{W}\mathfrak{y}}}{R_x}\\
&=I_3\frac{\partial^2\mathcal{U}_0}{\partial t^2}+I_4\frac{\partial^2\mathcal{U}_1}{\partial t^2}+I_5\frac{\partial^2\mathcal{U}_2}{\partial t^2}+I_6\frac{\partial^2\mathcal{U}_3}{\partial t^2}\\
&\quad +I_7\frac{\partial^2\mathcal{U}_4}{\partial t^2}+I_8\frac{\partial^2\mathcal{U}_5}{\partial t^2},\\
\delta\mathcal{V}_3:\ & \frac{\partial \mathfrak{f}_{\mathfrak{x}\mathfrak{x}}}{\partial \mathfrak{x}}+\frac{\partial \mathfrak{f}_{\mathfrak{W}\mathfrak{x}}}{\partial \mathfrak{W}}-3\mathfrak{P}_{\mathfrak{x}\mathfrak{y}}+\frac{\mathfrak{f}_{\mathfrak{x}\mathfrak{y}}}{R_y}\\
&=I_3\frac{\partial^2\mathcal{V}_0}{\partial t^2}+I_4\frac{\partial^2\mathcal{V}_1}{\partial t^2}+I_5\frac{\partial^2\mathcal{V}_2}{\partial t^2}+I_6\frac{\partial^2\mathcal{V}_3}{\partial t^2}\\
&\quad +I_7\frac{\partial^2\mathcal{V}_4}{\partial t^2}+I_8\frac{\partial^2\mathcal{V}_5}{\partial t^2},\\
\delta\mathcal{W}_3:\ & \frac{\partial \mathfrak{f}_{\mathfrak{W}\mathfrak{y}}}{\partial \mathfrak{W}}+\frac{\partial \mathfrak{f}_{\mathfrak{x}\mathfrak{y}}}{\partial \mathfrak{x}}-3\mathfrak{P}_{\mathfrak{y}\mathfrak{y}}-\frac{\mathfrak{f}_{\mathfrak{W}\mathfrak{W}}}{R_x}-\frac{\mathfrak{f}_{\mathfrak{x}\mathfrak{x}}}{R_y}\\
&=I_3\frac{\partial^2\mathcal{W}_0}{\partial t^2}+I_4\frac{\partial^2\mathcal{W}_1}{\partial t^2}+I_5\frac{\partial^2\mathcal{W}_2}{\partial t^2}+I_6\frac{\partial^2\mathcal{W}_3}{\partial t^2}\\
&\quad +I_7\frac{\partial^2\mathcal{W}_4}{\partial t^2}+I_8\frac{\partial^2\mathcal{W}_5}{\partial t^2},\\
\delta\mathcal{U}_4:\ & \frac{\partial \mathfrak{R}_{\mathfrak{W}\mathfrak{W}}}{\partial \mathfrak{W}}+\frac{\partial \mathfrak{R}_{\mathfrak{W}\mathfrak{x}}}{\partial \mathfrak{x}}-4\mathfrak{f}_{\mathfrak{W}\mathfrak{y}}+\frac{\mathfrak{R}_{\mathfrak{W}\mathfrak{y}}}{R_x}\\
&=I_4\frac{\partial^2\mathcal{U}_0}{\partial t^2}+I_5\frac{\partial^2\mathcal{U}_1}{\partial t^2}+I_6\frac{\partial^2\mathcal{U}_2}{\partial t^2}+I_7\frac{\partial^2\mathcal{U}_3}{\partial t^2}\\
&\quad +I_8\frac{\partial^2\mathcal{U}_4}{\partial t^2}+I_9\frac{\partial^2\mathcal{U}_5}{\partial t^2},\\
\delta\mathcal{V}_4:\ & \frac{\partial \mathfrak{R}_{\mathfrak{x}\mathfrak{x}}}{\partial \mathfrak{x}}+\frac{\partial \mathfrak{R}_{\mathfrak{W}\mathfrak{x}}}{\partial \mathfrak{W}}-4\mathfrak{f}_{\mathfrak{x}\mathfrak{y}}+\frac{\mathfrak{R}_{\mathfrak{x}\mathfrak{y}}}{R_y}\\
&=I_4\frac{\partial^2\mathcal{V}_0}{\partial t^2}+I_5\frac{\partial^2\mathcal{V}_1}{\partial t^2}+I_6\frac{\partial^2\mathcal{V}_2}{\partial t^2}+I_7\frac{\partial^2\mathcal{V}_3}{\partial t^2}\\
&\quad +I_8\frac{\partial^2\mathcal{V}_4}{\partial t^2}+I_9\frac{\partial^2\mathcal{V}_5}{\partial t^2},\\
\delta\mathcal{W}_4:\ & \frac{\partial \mathfrak{R}_{\mathfrak{W}\mathfrak{y}}}{\partial \mathfrak{W}}+\frac{\partial \mathfrak{R}_{\mathfrak{x}\mathfrak{y}}}{\partial \mathfrak{x}}-4\mathfrak{f}_{\mathfrak{y}\mathfrak{y}}-\frac{\mathfrak{R}_{\mathfrak{W}\mathfrak{W}}}{R_x}-\frac{\mathfrak{R}_{\mathfrak{x}\mathfrak{x}}}{R_y}\\
&=I_4\frac{\partial^2\mathcal{W}_0}{\partial t^2}+I_5\frac{\partial^2\mathcal{W}_1}{\partial t^2}+I_6\frac{\partial^2\mathcal{W}_2}{\partial t^2}+I_7\frac{\partial^2\mathcal{W}_3}{\partial t^2}\\
&\quad +I_8\frac{\partial^2\mathcal{W}_4}{\partial t^2}+I_9\frac{\partial^2\mathcal{W}_5}{\partial t^2},\\
\delta\mathcal{U}_5:\ & \frac{\partial \mathfrak{S}_{\mathfrak{W}\mathfrak{W}}}{\partial \mathfrak{W}}+\frac{\partial \mathfrak{S}_{\mathfrak{W}\mathfrak{x}}}{\partial \mathfrak{x}}-5\mathfrak{R}_{\mathfrak{W}\mathfrak{y}}+\frac{\mathfrak{S}_{\mathfrak{W}\mathfrak{y}}}{R_x}\\
&=I_5\frac{\partial^2\mathcal{U}_0}{\partial t^2}+I_6\frac{\partial^2\mathcal{U}_1}{\partial t^2}+I_7\frac{\partial^2\mathcal{U}_2}{\partial t^2}+I_8\frac{\partial^2\mathcal{U}_3}{\partial t^2}
\end{aligned}
\tag{17}
$$

$$
\begin{aligned}
&+I_9\frac{\partial^2\mathcal{U}_4}{\partial t^2}+I_{10}\frac{\partial^2\mathcal{U}_5}{\partial t^2},\\
\delta\mathcal{V}_5:\ &\frac{\partial\mathfrak{S}_{\mathfrak{x}\mathfrak{x}}}{\partial\mathfrak{X}}+\frac{\partial\mathfrak{S}_{\mathfrak{W}\mathfrak{x}}}{\partial\mathfrak{W}}-5\mathfrak{R}_{\mathfrak{x}\mathfrak{y}}+\frac{\mathfrak{S}_{\mathfrak{x}\mathfrak{y}}}{R_y}\\
&=I_5\frac{\partial^2\mathcal{V}_0}{\partial t^2}+I_6\frac{\partial^2\mathcal{V}_1}{\partial t^2}+I_7\frac{\partial^2\mathcal{V}_2}{\partial t^2}+I_8\frac{\partial^2\mathcal{V}_3}{\partial t^2}\\
&+I_9\frac{\partial^2\mathcal{V}_4}{\partial t^2}+I_{10}\frac{\partial^2\mathcal{V}_5}{\partial t^2},\\
\delta\mathcal{W}_5:\ &\frac{\partial\mathfrak{S}_{\mathfrak{W}\mathfrak{y}}}{\partial\mathfrak{W}}+\frac{\partial\mathfrak{S}_{\mathfrak{x}\mathfrak{y}}}{\partial\mathfrak{X}}-5\mathfrak{R}_{\mathfrak{y}\mathfrak{y}}-\frac{\mathfrak{S}_{\mathfrak{W}\mathfrak{W}}}{R_x}-\frac{\mathfrak{S}_{\mathfrak{x}\mathfrak{x}}}{R_y}\\
&=I_5\frac{\partial^2\mathcal{W}_0}{\partial t^2}+I_6\frac{\partial^2\mathcal{W}_1}{\partial t^2}+I_7\frac{\partial^2\mathcal{W}_2}{\partial t^2}+I_8\frac{\partial^2\mathcal{W}_3}{\partial t^2}\\
&+I_9\frac{\partial^2\mathcal{W}_4}{\partial t^2}+I_{10}\frac{\partial^2\mathcal{W}_5}{\partial t^2},\\
\delta\Phi:\ &\int\left\{\frac{\partial D_{\mathfrak{W}}}{\partial\mathfrak{W}}cos(\beta\mathfrak{Y})+\frac{\partial D_{\mathfrak{x}}}{\partial\mathfrak{W}}cos(\beta\mathfrak{Y})\right.\\
&\qquad\left.+\beta\,sin(\beta\mathfrak{Y})\,D_{\mathfrak{y}}\right\}d\mathfrak{Y}=0.
\end{aligned}
\tag{17}
$$

The involved terms in Eq. (17) would be formulated as

$$
\begin{aligned}
&\{\mathfrak{N}_{ij},\mathfrak{M}_{ij},\mathfrak{P}_{ij},\mathfrak{F}_{ij},\mathfrak{R}_{ij},\mathfrak{S}_{ij}\}\\
&=\int\{1,\mathfrak{Y},\mathfrak{Y}^2,\mathfrak{Y}^3,\mathfrak{Y}^4,\mathfrak{Y}^5\}\sigma_{ijc}d\mathfrak{Y},i,j=\mathfrak{W},\mathfrak{X},\mathfrak{Y},\\
&\{I_0,I_1,I_2,I_3,I_4,I_5,I_6,I_7,I_8,I_9,I_{10}\}\\
&=\int\{1,\mathfrak{Y},\mathfrak{Y}^2,\mathfrak{Y}^3,\mathfrak{Y}^4,\mathfrak{Y}^5,\mathfrak{Y}^6,\mathfrak{Y}^7,\mathfrak{Y}^8,\mathfrak{Y}^9,\mathfrak{Y}^{10}\}\rho d\mathfrak{Y}.
\end{aligned}
\tag{18}
$$

Moreover, Eq. (19) formulates the system's basic boundary conditions

$$
\begin{aligned}
&\delta\mathcal{U}_0:\ \mathfrak{N}_{\mathfrak{W}\mathfrak{W}}\hat{n}_{\mathfrak{W}}+\mathfrak{N}_{\mathfrak{W}\mathfrak{x}}\hat{n}_{\mathfrak{x}}=0,\\
&\delta\mathcal{V}_0:\ \mathfrak{N}_{\mathfrak{W}\mathfrak{x}}\hat{n}_{\mathfrak{W}}+\mathfrak{N}_{\mathfrak{x}\mathfrak{x}}\hat{n}_{\mathfrak{x}}=0,\\
&\delta\mathcal{W}_0:\ \left(\mathfrak{N}_{\mathfrak{W}\mathfrak{y}}-\mathfrak{N}_p\frac{\partial\mathcal{W}_0}{\partial\mathfrak{W}}\right)\hat{n}_{\mathfrak{W}}\\
&\qquad+\left(\mathfrak{N}_{\mathfrak{x}\mathfrak{y}}-\mathfrak{N}_p\frac{\partial\mathcal{W}_0}{\partial\mathfrak{X}}\right)\hat{n}_{\mathfrak{x}}=0,\\
&\delta\mathcal{U}_1:\ \mathfrak{M}_{\mathfrak{W}\mathfrak{W}}\hat{n}_{\mathfrak{W}}+\mathfrak{M}_{\mathfrak{W}\mathfrak{x}}\hat{n}_{\mathfrak{x}}=0,\\
&\delta\mathcal{V}_1:\ \mathfrak{M}_{\mathfrak{W}\mathfrak{x}}\hat{n}_{\mathfrak{W}}+\mathfrak{M}_{\mathfrak{x}\mathfrak{x}}\hat{n}_{\mathfrak{x}}=0,\\
&\delta\mathcal{W}_1:\ \mathfrak{M}_{\mathfrak{W}\mathfrak{y}}\hat{n}_{\mathfrak{W}}+\mathfrak{M}_{\mathfrak{x}\mathfrak{y}}\hat{n}_{\mathfrak{x}}=0,\\
&\delta\mathcal{U}_2:\ \mathfrak{P}_{\mathfrak{W}\mathfrak{W}}\hat{n}_{\mathfrak{W}}+\mathfrak{P}_{\mathfrak{W}\mathfrak{x}}\hat{n}_{\mathfrak{x}}=0,\\
&\delta\mathcal{V}_2:\ \mathfrak{P}_{\mathfrak{W}\mathfrak{x}}\hat{n}_{\mathfrak{W}}+\mathfrak{P}_{\mathfrak{x}\mathfrak{x}}\hat{n}_{\mathfrak{x}}=0,\\
&\delta\mathcal{W}_2:\ \mathfrak{P}_{\mathfrak{W}\mathfrak{y}}\hat{n}_{\mathfrak{W}}+\mathfrak{P}_{\mathfrak{x}\mathfrak{y}}\hat{n}_{\mathfrak{x}}=0,\\
&\delta\mathcal{U}_3:\ \mathfrak{F}_{\mathfrak{W}\mathfrak{W}}\hat{n}_{\mathfrak{W}}+\mathfrak{F}_{\mathfrak{W}\mathfrak{x}}\hat{n}_{\mathfrak{x}}=0,\\
&\delta\mathcal{V}_3:\ \mathfrak{F}_{\mathfrak{W}\mathfrak{x}}\hat{n}_{\mathfrak{W}}+\mathfrak{F}_{\mathfrak{x}\mathfrak{x}}\hat{n}_{\mathfrak{x}}=0,\\
&\delta\mathcal{W}_3:\ \mathfrak{F}_{\mathfrak{W}\mathfrak{y}}\hat{n}_{\mathfrak{W}}+\mathfrak{F}_{\mathfrak{x}\mathfrak{y}}\hat{n}_{\mathfrak{x}}=0,\\
&\delta\mathcal{U}_4:\ \mathfrak{R}_{\mathfrak{W}\mathfrak{W}}\hat{n}_{\mathfrak{W}}+\mathfrak{R}_{\mathfrak{W}\mathfrak{x}}\hat{n}_{\mathfrak{x}}=0,\\
&\delta\mathcal{V}_4:\ \mathfrak{R}_{\mathfrak{W}\mathfrak{x}}\hat{n}_{\mathfrak{W}}+\mathfrak{R}_{\mathfrak{x}\mathfrak{x}}\hat{n}_{\mathfrak{x}}=0,\\
&\delta\mathcal{W}_4:\ \mathfrak{R}_{\mathfrak{W}\mathfrak{y}}\hat{n}_{\mathfrak{W}}+\mathfrak{R}_{\mathfrak{x}\mathfrak{y}}\hat{n}_{\mathfrak{x}}=0,\\
&\delta\mathcal{U}_5:\ \mathfrak{S}_{\mathfrak{W}\mathfrak{W}}\hat{n}_{\mathfrak{W}}+\mathfrak{S}_{\mathfrak{W}\mathfrak{x}}\hat{n}_{\mathfrak{x}}=0,\\
&\delta\mathcal{V}_5:\ \mathfrak{S}_{\mathfrak{W}\mathfrak{x}}\hat{n}_{\mathfrak{W}}+\mathfrak{S}_{\mathfrak{x}\mathfrak{x}}\hat{n}_{\mathfrak{x}}=0,\\
&\delta\mathcal{W}_5:\ \mathfrak{S}_{\mathfrak{W}\mathfrak{y}}\hat{n}_{\mathfrak{W}}+\mathfrak{S}_{\mathfrak{x}\mathfrak{y}}\hat{n}_{\mathfrak{x}}=0,
\end{aligned}
\tag{19}
$$

3. Numerical solution

Below, a comprehensive explanation of the necessary procedures to use DQA as the numerical solution is provided.

3.1 Differential quadrature approach (DQA)

Through DQA, the p^{th} derivative of $f(\mathfrak{W})$ as a one-dimensional function can be derived as

$$
\frac{\partial^p f(\mathfrak{W})}{\partial\mathfrak{W}^p}=\sum_{j=1}^{\mathfrak{N}_{\mathfrak{W}}}A_{ij}^{(p)}f(\mathfrak{W})\qquad\text{for}\quad i=1,2,\dots,\mathfrak{N}_{\mathfrak{W}}\quad\text{and}\quad p=1,2,\dots,\mathfrak{N}_{\mathfrak{W}}-1.
\tag{20}
$$

where $A_{ij}^{(p)}$ shows the weight coefficients of the i^{th} grid-point $(j=1,2,\dots,\mathfrak{N}_{\mathfrak{W}})$ and $\mathfrak{N}_{\mathfrak{W}}$ represents the total number of grid-points.

By means of Eq. (21), one can formulate $A_{ij}^{(p)}$ for $i\neq j$ as

$$
A_{ij}^{(p)}=n\left(A_{ii}^{(p-1)}A_{ij}^{(1)}-\frac{A_{ij}^{(p-1)}}{\mathfrak{W}_i-\mathfrak{W}_j}\right),\qquad p=2,3,\dots,\mathfrak{N}_{\mathfrak{W}}-1\quad\text{and}\quad i,j=1,2,\dots,\mathfrak{N}_{\mathfrak{W}},
\tag{21}
$$

where $A_{ij}^{(1)}$ is determined by subsequent relation

$$
A_{ij}^{(1)}=\frac{\mathfrak{M}^{(1)}(\mathfrak{W}_i)}{(\mathfrak{W}_i-\mathfrak{W}_j)\mathfrak{M}^{(1)}(\mathfrak{W}_j)},i,j=1,2,\dots,\mathfrak{N}_{\mathfrak{W}},
\tag{22}
$$

One can employ the subsequent relation to acquire $A_{ii}^{(p)}$

$$
A_{ii}^{(p)}=-\sum_{j=1,j\neq i}^{\mathfrak{N}}A_{ij}^{(p)},\quad i=2,3,\dots,\mathfrak{N}_{\mathfrak{W}}\qquad\text{and}\quad p=1,2,\dots,\mathfrak{N}_{\mathfrak{W}}-1
\tag{23}
$$

$\mathfrak{M}^{(1)}$ in Eq. (22) would be obtained as

$$
\mathfrak{M}^{(1)}(\mathfrak{W}_k)=-\sum_{j=1,j\neq k}^{\mathfrak{N}_{\mathfrak{W}}}(\mathfrak{W}_k-\mathfrak{W}_j),\qquad\text{for}\quad k=1,2,3,\dots,\mathfrak{N}_{\mathfrak{W}}.
\tag{24}
$$

3.2 Two-dimensional approximation

On the basis of DQA, the first two derivatives for $f(\mathfrak{W},\mathfrak{X})$ as a two-dimensional function would be obtained as follows (Rahimi *et al*. 2020)

$$
\begin{aligned}
&\left.\frac{\partial f}{\partial\mathfrak{W}}\right|_{\mathfrak{W}=\mathfrak{W}_i,\mathfrak{x}=\mathfrak{x}_j}=\sum_{p=1}^{\mathfrak{N}_{\mathfrak{W}}}\sum_{k=1}^{\mathfrak{N}_{\mathfrak{x}}}A_{ip}^{\mathfrak{W}}I_{pk}^{\mathfrak{x}}f_{kj},\\
&\left.\frac{\partial f}{\partial\mathfrak{X}}\right|_{\mathfrak{W}=\mathfrak{W}_i,\mathfrak{x}=\mathfrak{x}_j}=\sum_{p=1}^{\mathfrak{N}_{\mathfrak{W}}}\sum_{k=1}^{\mathfrak{N}_{\mathfrak{x}}}I_{ip}^{\mathfrak{W}}A_{pk}^{\mathfrak{x}}f_{kj},\\
&\frac{\partial}{\partial\mathfrak{W}}\left(\left.\frac{\partial f}{\partial\mathfrak{X}}\right|_{\mathfrak{W}=\mathfrak{W}_i,\mathfrak{x}=\mathfrak{x}_j}\right)=\sum_{p=1}^{\mathfrak{N}_{\mathfrak{W}}}\sum_{k=1}^{\mathfrak{N}_{\mathfrak{x}}}A_{ip}^{\mathfrak{W}}A_{pk}^{\mathfrak{x}}f_{kj},\\
&\left.\frac{\partial^2 f}{\partial\mathfrak{W}^2}\right|_{\mathfrak{W}=\mathfrak{W}_i,\mathfrak{x}=\mathfrak{x}_j}=\sum_{p=1}^{\mathfrak{N}_{\mathfrak{W}}}\sum_{k=1}^{\mathfrak{N}_{\mathfrak{x}}}B_{ip}^{\mathfrak{W}}I_{pk}^{\mathfrak{x}}f_{kj},\\
&\left.\frac{\partial^2 f}{\partial\mathfrak{X}^2}\right|_{\mathfrak{W}=\mathfrak{W}_i,\mathfrak{x}=\mathfrak{x}_j}=\sum_{p=1}^{\mathfrak{N}_{\mathfrak{W}}}\sum_{k=1}^{\mathfrak{N}_{\mathfrak{x}}}I_{ip}^{\mathfrak{W}}B_{pk}^{\mathfrak{x}}f_{kj}.
\end{aligned}
\tag{25}
$$

Here $A_{pk}^{\mathfrak{x}}$, $A_{ip}^{\mathfrak{W}}$, $B_{pk}^{\mathfrak{x}}$, and $B_{ip}^{\mathfrak{W}}$ represent the weight coefficients.

Additionally, $\mathfrak{N}_{\mathfrak{x}}$, and $\mathfrak{N}_{\mathfrak{W}}$ are in order the number of grid-points picked through the latitudinal and longitudinal orientations**.** Also, $I_{ip}^{\mathfrak{W}}$, $I_{pk}^{\mathfrak{x}}$, $I_{ip}^{\mathfrak{W}}$, and $I_{pk}^{\mathfrak{x}}$ are identity tensors. Based on the implementation of Chebyshev–Gauss–Lobatto function, the coordination of the grid-points $(\mathfrak{W}_i, \mathfrak{x}_j)$ are formulated as

$$\begin{aligned}\mathfrak{W}_i &= \frac{a}{2}\left(1 - cos\left(\frac{(i-1)}{(\mathfrak{N}_{\mathfrak{W}}-1)}\pi\right)\right) i = 1,2,3,\ldots,\mathfrak{N}_{\mathfrak{W}},\\ \mathfrak{x}_j &= \frac{b}{2}\left(1 - cos\left(\frac{(j-1)}{(\mathfrak{N}_{\mathfrak{x}}-1)}\pi\right)\right) j = 1,2,3,\ldots,\mathfrak{N}_{\mathfrak{x}}.\end{aligned} \tag{26}$$

Therefore, by replacing Eqs. (25) and (18) with equation (17), we get the following equation

$$\left[[\mathcal{M}_{ij}]\{\ddot{X}\} + [\mathcal{K}_{ij}]\{X\} = F_k(t),\right. \tag{27}$$

The equations of motion may be determined by using the stiffness matrix $[\mathcal{K}_{ij}]$, mass matrix $[\mathcal{M}_{ij}]$, and nodal time-dependent force vector F_k, as outlined in Eq. (27). The following structure was used to express the limits or constraints. By using the Laplace transform (Nguyen *et al.* 2022) to Eq. (27) with different boundary conditions, the following relationships are derived.

$$[\mathcal{M}_{ij}]\{S^2X(s)\} + [\mathcal{K}_{ij}]\{X(s)\} = F_k(s), \tag{28}$$

The displacement for each layer may be obtained by solving Eq. (28) using the layer-wise technique and the Laplace transform (Nguyen *et al*. 2022). The equations (8) and (9) will provide the displacements and stress of the doubly curved panel in a transverse position. The displacements and stresses are determined over time by using the Laplace transform inversion on Dubner and Abate's modified formulation (Durbin 1974). Therefore, Eq. (29) is the mathematical formula used to carry out the inverse Laplace transform in this research.

$$\not{f}(t) = \frac{2e^{at}}{T}\left[-\frac{A_0}{2} + \sum_{k=0}^{\infty}\left(A_k cos\left(\frac{2k\pi t}{T}\right) - B_k sin\left(\frac{2k\pi t}{T}\right)\right)\right], \tag{29}$$

here

$$\begin{aligned}&A_0 = Re[F(a)], \quad A_k = Re\left[F\left(a + i\frac{2k\pi}{T}\right)\right],\\ &B_k = Im\left[F\left(a + i\frac{2k\pi}{T}\right)\right], \quad S = a + i\frac{2k\pi}{T}, \quad aT = 5.\end{aligned} \tag{30}$$

3.3 Deep-learning solution

The application of deep learning solutions for estimating deflection in smart structures represents a significant advancement in the field of structural health monitoring and control. Smart structures are equipped with sensors, actuators, and control systems that enable them to sense, process, and respond to changes in their environment or operating conditions. Deflection, which refers to the displacement or deformation of a structure under load, is a critical parameter that directly impacts the structural integrity, performance, and safety. Traditional methods for estimating deflection in structures often rely on analytical models, finite element analysis, or empirical equations, which may have limitations in accuracy, computational efficiency, or robustness, especially for complex or nonlinear systems. Deep learning, particularly deep neural networks (DNNs), offers a promising alternative by leveraging the power of artificial intelligence to learn complex patterns and relationships from data. The application of deep learning solutions to estimate deflection in smart structures involves several key steps:

1. **Data Collection:** Large datasets of structural response data, including deflection measurements, sensor readings, and environmental conditions, are collected through sensors embedded in the structure or obtained from simulations and experiments.
2. **Data Preprocessing:** The collected data is preprocessed to remove noise, outliers, and inconsistencies, and to prepare it for input into the deep learning model. This may involve normalization, scaling, feature extraction, and data augmentation techniques.
3. **Model Development:** Deep learning models, such as deep neural networks (DNNs), convolutional neural networks (CNNs), or recurrent neural networks (RNNs), are designed and trained using the preprocessed data. The model architecture, including the number of layers, neurons, activation functions, and optimization algorithms, is selected based on the specific characteristics of the problem and the available data.
4. **Training and Validation:** The deep learning model is trained using the labeled dataset, where the input data corresponds to sensor measurements or environmental factors, and the output data corresponds to deflection measurements. The model learns to map the input data to the corresponding deflection values through iterative optimization of its parameters.
5. **Model Evaluation:** The trained model is evaluated using a separate validation dataset to assess its performance in terms of accuracy, generalization, and robustness. Various metrics, such as mean squared error (MSE), root mean squared error (RMSE), and coefficient of determination (R^2), are used to quantify the model's predictive capability.
6. **Deployment and Integration:** Once the deep learning model has been trained and validated, it can be deployed and integrated into the smart structure's monitoring and control system. Real-time deflection estimation can be performed using sensor data acquired during operation, allowing for timely detection of structural anomalies, damage, or degradation.

Overall, the application of deep learning solutions to estimate deflection in smart structures offers several advantages, including improved accuracy, efficiency, and scalability compared to traditional methods. By harnessing the power of artificial intelligence, engineers and researchers can develop more reliable, adaptive, and resilient structural health monitoring and control systems for a wide range of applications, including civil infrastructure, aerospace, automotive, and manufacturing. Here are some advantages and disadvantages of using deep learning algorithms, such as deep neural networks (DNNs), for estimating the transient dynamics of a structure:

Advantages:

1. **Complex Pattern Recognition:** Deep learning algorithms excel at learning complex patterns and relationships from data, making them well-suited for capturing the nonlinear behavior and dynamics of structures.
2. **Data-Driven Approach:** Deep learning algorithms are inherently data-driven, allowing them to learn directly from large datasets of structural response data without relying heavily on predefined models or equations.
3. **Feature Extraction:** Deep learning algorithms can automatically extract relevant features from raw sensor data, reducing the need for manual feature engineering and potentially uncovering hidden correlations or insights.
4. **Adaptability:** DNNs can adapt and learn from new data, enabling them to continuously improve and update their predictions over time as more data becomes available or as the structural behavior evolves.
5. **Scalability:** Deep learning algorithms can scale to handle large and complex datasets, making them suitable for analyzing high-dimensional sensor data collected from multiple sensors distributed throughout a structure.

Disadvantages:

1. **Data Requirements:** Deep learning algorithms typically require large amounts of labeled training data to effectively learn the underlying patterns and dynamics of a structure. Acquiring and labeling such datasets can be time-consuming and expensive.
2. **Black Box Nature:** DNNs are often considered "black box" models, meaning that they provide accurate predictions but offer limited interpretability or insights into the underlying physical mechanisms driving the structural dynamics.
3. **Overfitting:** Deep learning models are susceptible to overfitting, especially when trained on noisy or insufficient data. Overfitting occurs when the model learns to memorize the training data rather than generalize to unseen data, leading to poor performance on new data.
4. **Computational Resources:** Training deep learning models, particularly large and complex DNN architectures, requires significant computational resources, including high-performance GPUs or TPUs, as well as substantial memory and storage capacity.
5. **Hyperparameter Tuning:** Deep learning models have several hyperparameters that need to be tuned, such as the number of layers, neurons, activation functions, and learning rates. Finding the optimal set of hyperparameters can be challenging and time-consuming.

Overall, while deep learning algorithms offer significant potential for estimating the transient dynamics of structures, it is essential to carefully consider their advantages and disadvantages and to tailor their use to the specific requirements and constraints of the application at hand. Here's a mathematical modeling overview of the deep learning algorithm, particularly deep neural networks (DNNs), for estimating the transient dynamics of a structure: Let's denote the input dataset as X and the corresponding output (target) dataset as Y. Each row of the dataset represents a sample, and each column represents a feature or attribute. For example, the input dataset X may include sensor readings or measurements collected from various sensors installed on the structure, while the output dataset Y may include the corresponding transient deflection values of the structure. The goal of the DNN model is to learn a mapping function $f: X \to Y$ that accurately predicts the transient deflection of the structure given the input sensor data. This mapping function is represented by the parameters (weights and biases) of the neural network. The DNN model consists of multiple layers of interconnected neurons, including input layers, hidden layers, and output layers. Each neuron applies a linear transformation to the input data followed by a nonlinear activation function, such as the rectified linear unit (ReLU) or hyperbolic tangent (tanh) function. Mathematically, the forward pass of the DNN model can be represented as follows

$$\begin{aligned}
&[Z]^{[1]} = [W]^{[1]}X + [b]^{[1]},\\
&[A]^{[1]} = [g]^{[1]}\left([Z]^{[1]}\right),\\
&[Z]^{[2]} = [W]^{[2]}[A]^{[1]} + [b]^{[2]},\\
&[A]^{[2]} = [g]^{[2]}\left([Z]^{[2]}\right),\\
&\vdots\\
&[Z]^{[L]} = [W]^{[L]}[A]^{[L-1]} + [b]^{[L]},\\
&\hat{Y} = [A]^{[L]} = [g]^{[L]}\left([Z]^{[L]}\right).
\end{aligned} \tag{31}$$

During the training phase, the DNN model learns the optimal values of the parameters (weights and biases) by minimizing a loss function, which measures the discrepancy between the predicted output $\hat{Y}$ and the actual output Y. This optimization process is typically performed using gradient-based optimization algorithms such as stochastic gradient descent (SGD) or Adam. Once the model is trained, it can be used to predict the transient deflection of the structure for new input data that was not seen during training. Overall, the mathematical modeling of the DNN algorithm for estimating the transient dynamics of a structure involves defining the architecture of the neural network, specifying the activation functions, and optimizing the model parameters to minimize the prediction error. Here's a simple MATLAB code to demonstrate how you

```
% Load your dataset (X, Y)
load('your_dataset.mat');
% Define the architecture of the neural network
layers = [
    fullyConnectedLayer(32)     % Fully connected layer with 32 neurons
    reluLayer                   % ReLU activation layer
    fullyConnectedLayer(16)     % Fully connected layer with 16 neurons
    reluLayer                   % ReLU activation layer
    fullyConnectedLayer(1)      % Output layer with 1 neuron (for regression)
];
% Specify training options
options = trainingOptions('adam', ...        % Optimization algorithm
    'MaxEpochs', 50, ...                      % Maximum number of epochs
    'MiniBatchSize', 32, ...                  % Mini-batch size
    'InitialLearnRate', 0.001, ...            % Initial learning rate
    'LearnRateSchedule', 'piecewise', ...     % Learning rate schedule
    'LearnRateDropFactor', 0.1, ...           % Learning rate drop factor
    'LearnRateDropPeriod', 10, ...            % Learning rate drop period
    'Shuffle', 'every-epoch', ...             % Shuffle data every epoch
    'Verbose', true);                         % Display training progress
% Train the neural network
net = trainNetwork(X_train, Y_train, layers, options);

% Predict using the trained network
Y_pred = predict(net, X_test);

% Evaluate the performance (optional)
mse = mean((Y_pred - Y_test).^2);
fprintf('Mean Squared Error (MSE): %.4f\n', mse);
```

Fig. 3 A Matlab code for deep learning solutions to estimate the deflection in smart structures

can create and train a basic deep neural network (DNN) using MATLAB's built-in functions. This code assumes that you have a dataset consisting of input features (X) and corresponding target labels (Y) for training the network. Fig. 3 shows a matlab code for deep learning solutions to estimate the deflection in smart structures.

4. Results and discussion

In this section, the influences of some geometrical and physical parameters on the presented smart structure is shown. First a verification between the results of current work and published articles are presented. Then a parametric result is presented. Finally, the results of presented deep learning algorithm is presented.

4.1 Validation

A verification between the outcomes of presented work and published articles (Gilhooley *et al*. 2007, Lee *et al*. 2009, Nguyen-Xuan *et al*. 2011) is presented in Table 3 to compare the results of non-dimensional center deflection of square Al/ZrO_2-1 plates under a uniform load. As is presented, the results are compared for various FG power index and boundary conditions. All in all, can be concluded that the results of presented study is in good agreement with the outcomes of Refs. (Gilhooley *et al*. 2007, Lee *et al*. 2009, Nguyen-Xuan *et al*. 2011).

4.2 Parametric results

In this subsection, the influences of some geometrical and physical parameters on the presented smart structure are shown. Fig. 4 shows the impact of boundary domain on the dynamic deflection properties of the presented smart structure at various time domains. As is seen, an increase in the time results in fluctuation in response. It means that by increasing the time domain, up and down in the deflection of the current smart structure can be seen. Also, selecting

Table 3 Non-dimensional center deflection of square Al/ZrO_2-1 plates under a uniform load

Boundary condition	Methods	*n*			
		0	**0.5**	**1**	**2**
SSSS	Present	0.1715	0.2317	0.2714	0.3119
	Nguyen-Xuan *et al*. (2011)	0.1703	0.2232	0.2522	0.2827
	Gilhooley *et al*. (2007)	0.1671	0.2505	0.2905	0.3280
	Lee *et al*. (2009)	0.1722	0.2403	0.2811	0.3221
CCCC	Present	0.0768	0.1062	0.1194	0.1396
	Nguyen-Xuan *et al*. (2011)	0.0777	0.1012	0.1152	0.1313
	Gilhooley *et al*. (2007)	0.0731	0.1034	0.1253	0.1444
	Lee *et al*. (2009)	0.0774	0.1073	0.1207	0.1404

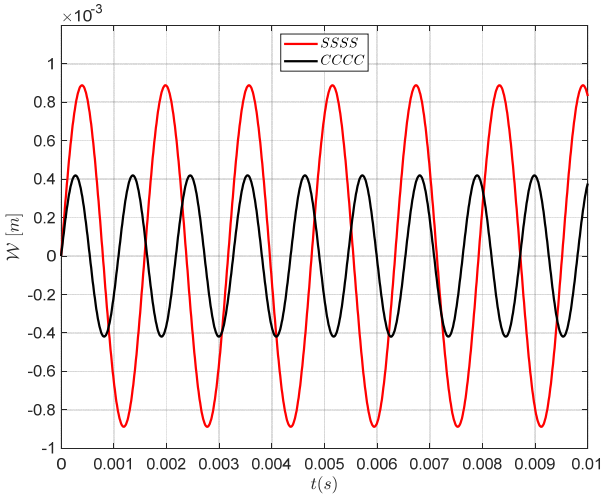

Fig. 4 The impact of boundary domain on the dynamic deflection properties of the presented smart structure at various time domains

clamped boundary conditions as the boundary edge of the presented system results in lower dynamic deflection in the current smart structure.

To understand about the impacts of duration time of applied load and type of GPL distribution patterns on the presented smart structure, Fig. 5 is appeared. As is observed, selecting GPL-UD as the GPL distribution pattern, has middle dynamic deflection at various duration times than other GPL distribution patterns. In other word, GPL-O, and GPL-X as the GPL distribution patterns result in highest and lowest dynamic deflection than GPL-UD as the GPL distribution pattern.

Fig. 6 illustrates the effects of the length time of the applied load and the weight percentage of GPLs on the smart structure under consideration. It is evident that choosing the median weight fraction of GPLs results in a moderate dynamic deflection at different durations compared to other weight fractions of GPLs. Put simply,

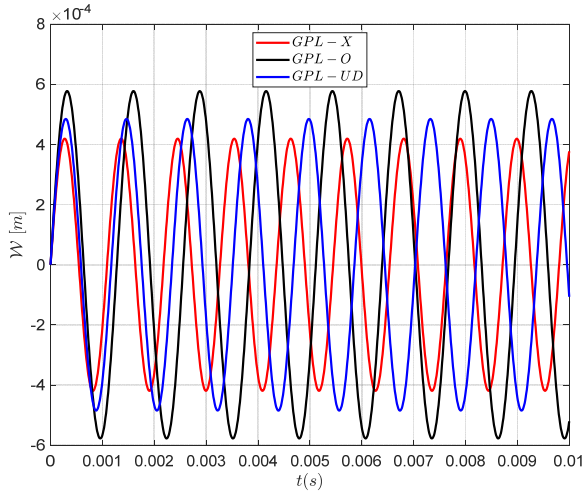

Fig. 5 The impacts of duration of applied load and type of GPL distribution patterns on the presented smart structure

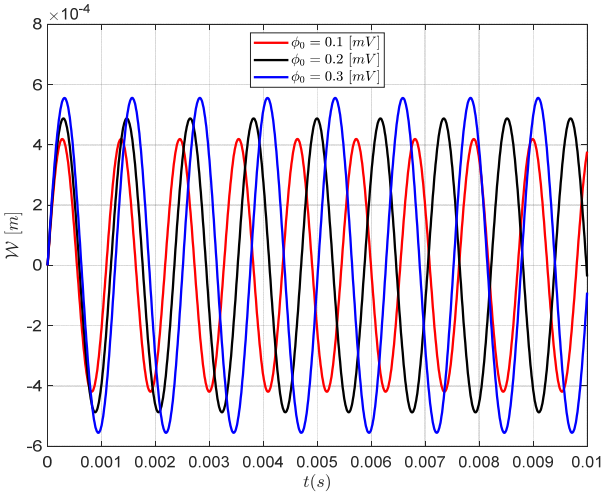

Fig. 7 The impacts of external electrical loading and duration time of applied loading on the presented smart structure

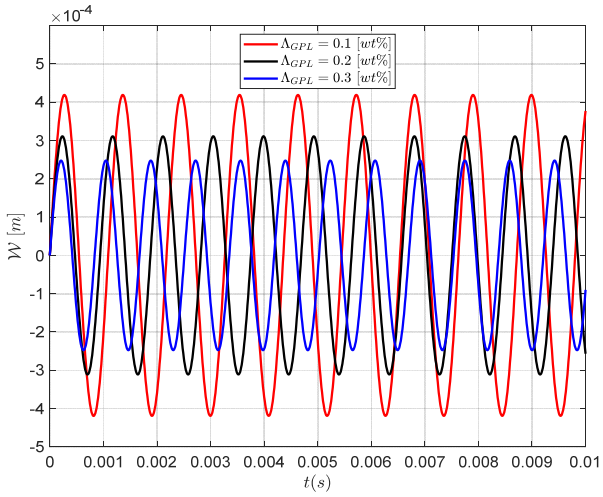

Fig. 6 The impacts of duration time of applied load and GPLs' weight fraction on the presented smart structure

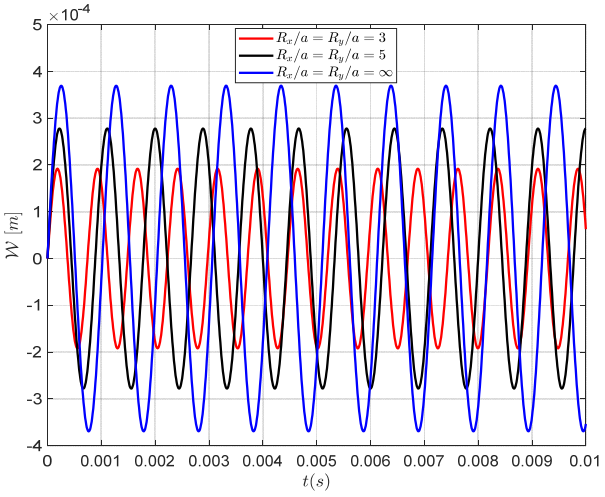

Fig. 8 The impacts of radius ratio and duration time of applied loading on the presented smart structure

smaller and higher weight fractions of GPLs lead to the largest and lowest dynamic deflection, respectively, compared to the weight fraction in the medium range.

The impacts of external electrical loading and duration time of applied loading on the presented smart structure is shown in Fig. 7. As is observed, by increasing the electrical applied loading on the current smart system, the dynamic deflection value increases. It means that by increasing the electrical applied loading on the current smart system, the stability in the system decreases. Also, by increasing the electrical applied loading on the current smart system, the fluctuation in the presented smart system in a specific value of the duration time decreases. It means that by increasing the electrical applied loading on the current smart system, the natural frequency of the smart structure decreases.

The effects of the radius ratio and duration time of the applied stress on the smart structure are shown in Fig. 8. It is evident that raising the radius ratio on the existing smart system leads to an increase in the dynamic deflection value. Increasing the radius ratio on the existing smart system leads to a loss in system stability. Moreover, by augmenting the radius ratio in the existing intelligent system, the variability in the shown intelligent system at a certain duration diminishes. Increasing the radius ratio of the smart structure leads to a drop in its natural frequency.

The effects of the b/a ratio and duration of applied loading on the smart structure are shown in Fig. 9. It can be noted that raising the ratio of b to a lead to an increase in the dynamic deflection of the present smart system. Increasing the ratio of b to a result in a loss in system stability. Moreover, by augmenting the ratio of b to a, the variability in the observed intelligent system at a certain duration diminishes. Increasing the ratio of b/a results in a reduction in the natural frequency of the smart structure.

The impacts of external applied excitation value and duration time of applied loading on the presented smart structure, Fig. 10 is appeared. As is shown by increasing the external applied excitation value the more fluctuation in

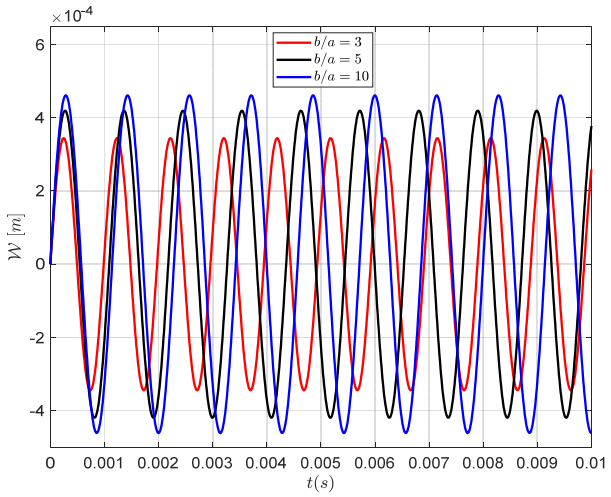

Fig. 9 The impacts of b/a and duration time of applied loading on the presented smart structure

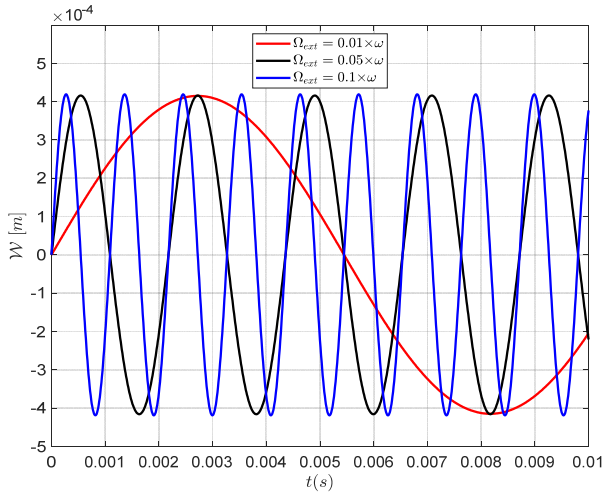

Fig. 10 The impacts of external applied excitation value and duration time of applied loading on the presented smart structure

response can be seen. It means that the stability in the system decreases.

4.3 Artificial intelligence algorithm results

The numerical analysis yields a dataset of 291 data points by utilizing known input and output parameters, as described in section 5.2. The dataset includes left and right boundary conditions, specifically two types: strict-strict and basic BC supported. Other quantities such as substrate data and external voltage are derived from the numerical results. The amplitude and bending information are obtained from the numerical data presented in Figs. 4-10. The PyTorch artificial intelligence training technique is straightforward. The collected data is randomly divided into three equal parts for training, validation, and testing phases. The number of network epochs (iterations) is determined based on the value of the loss function. The training data constitutes 80% of the dataset, while the remaining 20% is evenly split between validation and testing data.

Fig. 11 displays the number of epochs needed for training data in both the training and validation phases. Typically, once the loss-error curve reaches a stable state between the training and validation phases, it indicates that the network is trained. However, beyond this point, although the training error continues to decrease, the network becomes overfitted and only performs well on the training data. Consequently, the intelligence networks will produce unrealistic and inaccurate results for the validation data set and any future input data. Based on our observations, a minimum of 2100 epochs are required to have confidence in the results. Any epochs beyond this value will result in overfitting.

Fig. 12 depicts the prognostications of the intelligence network. It is evident that there is a strong correlation between the predictions made by the intelligence networks and the actual values. The maximum deformation process at the initial amplitude is assessed using the correlation value $R^2 = 0.9931$. The figure clearly demonstrates that dynamic deflection, when compared to other parameters, exhibits

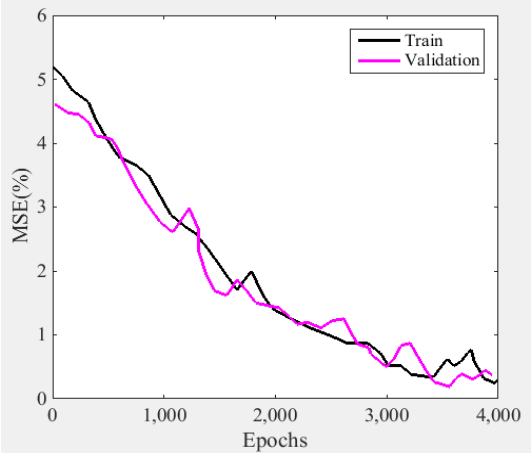

Fig. 11 The MSE value calculated by considering the number of epochs for each output obtained from the training and validation data sets

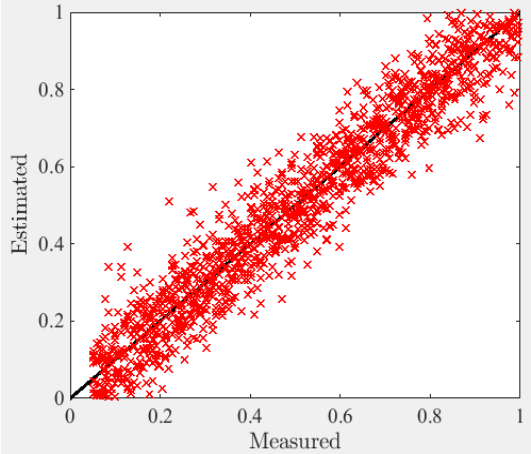

Fig. 12 The outcomes forecasted by the intelligence networks in relation to the numerical values of the solution

Table 4 Comparison between the dimensionless amplitude of intelligence networks (INs) and presented numerical simulation by changing R_x/a, and b/a parameters

b/a	R_x/a			
	1		5	
	DQM	INs	DQM	INs
1.5	-0.17264	-0.18148	-1.2548	-1.27166
2	-0.4548	-0.45566	-1.4996	-1.50822
2.5	-0.60664	-0.59622	-2.12704	-2.12118
3	-0.76224	-0.75407	-2.52784	-2.51622

a high level of agreement with the actual answer, as indicated by a R^2 value of 0.9931. So, employing learned parameters, we may provide fresh results of the given composite structure using intelligence networks.

Table 4 displays the outcomes of the latest DQM using intelligence networks to assess the amplitude of the smart structure in a dimensionless manner. The analysis reveals that the amplitude of the smart structure in the current system increases as the R_x/a parameter increases. Furthermore, the amplitude also increases with an increase in the b/a parameter. By comparing the results, it can be inferred that there is a significant level of agreement between the two methods.

5. Conclusions

There has been a steady increase in the trend towards designing smart buildings that can actively monitor and react to their surroundings. These smart structures have an important feature that is essential to maintaining the integrity and efficacy of the whole structure: they can predict deflection and react to it correctly. Conventional techniques for determining deflection often depend on intricate mathematical models and computational simulations, which may be resource- and time-intensive. Artificial intelligence (AI) algorithms have become a potent tool for controlling and anticipating deflection in intelligent systems in response to these difficulties. AI systems anticipate deflection precisely in real-time by using the vast amounts of data provided by sensors and actuators built into the structure. This allows the systems to identify intricate patterns and correlations. Artificial intelligence (AI) algorithms may be used to programme smart structures to automatically modify their form and behaviour in order to reduce bending and increase efficiency. According to this paradigm, "deflection-aware smart structures" are buildings that have AI algorithms installed in order to continually monitor and analyse deflection data in order to proactively identify any problems and take corrective action. These structures anticipate deflection in a variety of operating situations and environmental factors by using advanced artificial intelligence techniques including deep learning, reinforcement learning, and neural networks. There are several advantages of integrating AI algorithms into smart structures, such as increased accuracy, less computational complexity, and better flexibility in response to changing circumstances. Deflection-aware smart structures have the potential to enhance energy efficiency, durability, and service life in a variety of sectors, such as mechanical components, aeronautical systems, and civil infrastructure, by accurately predicting deflection and performing real-time alterations. To sum up, the development of deflection-aware smart structures is a major step in structural engineering that provides prospects to improve the efficiency, safety, and dependability of designed systems across all domains.

Acknowledgments

The authors extend their appreciation to King Saud University, Saudi Arabia for funding this work through Researchers Supporting Project number (RSP2024R305), King Saud University, Riyadh, Saudi Arabia.

References

Al Nuaimi, E., Al Neyadi, H., Mohamed, N. and Al-Jaroodi, J. (2015), "Applications of big data to smart cities", *J. Internet Servic. Applicat.*, **6**, 25. https://doi.org/10.1186/s13174-015-0041-5

Bhardwaj, K.K., Banyal, S., Sharma, D.K. and Al-Numay, W. (2022), "Internet of things based smart city design using fog computing and fuzzy logic", *Sustain. Cities Soc.*, **79**, 103712. https://doi.org/10.1016/j.scs.2022.103712

Bibri, S.E. and Krogstie, J. (2017a), "Smart sustainable cities of the future: An extensive interdisciplinary literature review", *Sustain. Cities Soc.*, **31**, 183-212. https://doi.org/10.1016/j.scs.2017.02.016

Bibri, S.E. and Krogstie, J. (2017b), "ICT of the new wave of computing for sustainable urban forms: Their big data and context-aware augmented typologies and design concepts", *Sustain. Cities Soc.*, **32**, 449-474. https://doi.org/10.1016/j.scs.2017.04.012

Cao, Y. and AlKubaisy, Z.M. (2022), "Integration of computer-based technology in smart environment in an EFL structures", *Smart Struct. Syst., Int. J.*, **29**(2), 375-387. https://doi.org/10.12989/sss.2022.29.2.375

Caragliu, A., Del Bo, C. and Nijkamp, P. (2013), "Smart cities in Europe", In: *Creating Smart-er Cities.*, **18**, 65-82.

Chase, J.G., Tomlinson, H., Rodgers, G.W., Xu, C., Avot, V. and Zhou, C. (2023), "Accuracy and robustness of hysteresis loop analysis in the identification and monitoring of plastic stiffness for highly nonlinear pinching structures", *Smart Struct. Syst., Int. J.*, **31**(2), 101-111. https://doi.org/10.12989/sss.2023.31.2.101

Chen, C.W. (2023), "Can smart cities bring happiness to promote sustainable development? Contexts and clues of subjective well-being and urban livability", *Develop. Built Environ.*, **13**, 100108. https://doi.org/10.1016/j.dibe.2022.100108

Chen, L., Xiong, H., He, Y., Li, X. and Kong, Q. (2022), "Monitoring moisture content of timber structures using PZT-enabled sensing and machine learning", *Smart Struct. Syst., Int. J.*, **29**(4), 589-598. https://doi.org/10.12989/sss.2022.29.4.589

Chen, C., Yang, H., Song, K., Liang, D., Zhang, Y. and Ni, J. (2023), "Dissolution feature differences of carbonate rock within hydro-fluctuation belt located in the Three Gorges Reservoir Area", *Eng. Geol.*, **327**, 107362. https://doi.org/10.1016/j.enggeo.2023.107362

Chu, Z., Cheng, M. and Yu, N.N. (2021), "A smart city is a less

polluted city", *Technological Forecasting and Social Change*., **172**, 121037. https://doi.org/10.1016/j.techfore.2021.121037

Durbin, F. (1974), "Numerical inversion of Laplace transforms: an efficient improvement to Dubner and Abate's method", *Comput. J.*, **17**, 371-376. https://doi.org/10.1093/comjnl/17.4.371

Feng, Q. and Liang, Y. (2022), "Development of piezoelectric-based technology for application in civil structural health monitoring", *Earthq. Res. Adv.*, **3**(2), 100154. https://doi.org/10.1016/j.eqrea.2022.100154

Feng, Y., Mohammadi, M., Wang, L., Rashidi, M. and Mehrabi, P. (2021), "Application of artificial intelligence to evaluate the fresh properties of self-consolidating concrete", *Mater.*, **14**, 4885. https://doi.org/10.3390/ma14174885

Firouzianhaji, A., Usefi, N., Samali, B. and Mehrabi, P. (2021), "Shake table testing of standard cold-formed steel storage rack", *Appl. Sci.*, **11**, 1821. https://doi.org/10.3390/app11041821

Gilhooley, D.F., Batra, R.C., Xiao, J.R., McCarthy, M.A. and Gillespie Jr, J.W. (2007), "Analysis of thick functionally graded plates by using higher-order shear and normal deformable plate theory and MLPG method with radial basis functions", *Compos. Struct.*, **80**, 539-552. https://doi.org/10.1016/j.compstruct.2006.07.007

Gordan, M., Sabbagh-Yazdi, S.R., Ismail, Z., Ghaedi, K., Carroll, P., McCrum, D. and Samali, B. (2022), "State-of-the-art review on advancements of data mining in structural health monitoring", *Measur.*, **193**, 110939. https://doi.org/10.1016/j.measurement.2022.110939

Guo, H. and Zhang, J. (2023), "Expansion of sandwich tubes with metal foam core under axial compression", *J. Appl. Mech.*, **90**, 051008. https://doi.org/10.1115/1.4056686

Guo, Y., Tang, Z. and Guo, J. (2020), "Could a smart city ameliorate urban traffic congestion? A quasi-natural experiment based on a smart city pilot program in China", *Sustainab.*, **12**, 2291. https://doi.org/10.3390/su12062291

Han, S., Zheng, D., Mehdizadeh, B., Nasr, E.A., Khandaker, M.U., Salman, M. and Mehrabi, P. (2023a), "Sustainable design of self-consolidating green concrete with partial replacements for cement through neural-network and fuzzy technique", *Sustainab.*, **15**, 4752. https://doi.org/10.3390/su15064752

Han, S., Zhu, Z., Mortazavi, M., El-Sherbeeny, A.M. and Mehrabi, P. (2023b), "Analytical assessment of the structural behavior of a specific composite floor system at elevated temperatures using a newly developed hybrid intelligence method", *Build.*, **13**, 799. https://doi.org/10.3390/buildings13030799

He, Z., Li, W., Salehi, H., Zhang, H., Zhou, H. and Jiao, P. (2022), "Integrated structural health monitoring in bridge engineering", *Automat. Constr.*, **136**, 104168. https://doi.org/10.1016/j.autcon.2022.104168

He, L., Maalla, A., Zhou, X. and Tang, H. (2024), "Buckling and post-buckling of anisogrid lattice-core sandwich plates with nanocomposite skins", *Thin-Wall. Struct.*, **199**, 111828. https://doi.org/10.1016/j.tws.2024.111828

Herath, H.M.K.K.M.B. and Mittal, M. (2022), "Adoption of artificial intelligence in smart cities: A comprehensive review", *Int. J. Inform. Manag. Data Insights.*, **2**, 100076. https://doi.org/10.1016/j.jjimei.2022.100076

Horne, J., Beddingfield, E., Knapp, M., Mitchell, S., Crawford, L., Mills, S.B., Wrist, A., Zhang, S. and Summers, R.M. (2020), "Caffeine and Theophylline Inhibit β-Galactosidase Activity and Reduce Expression in *Escherichia coli*", *ACS omega*, **5**, 32250-32255. https://doi.org/10.1021/acsomega.0c03909

Hu, D., Sun, H., Mehrabi, P., Ali, Y.A. and Al-Razgan, M. (2023), "Application of artificial intelligence technique in optimization and prediction of the stability of the walls against wind loads in building design", *Mech. Adv. Mater. Struct.*, 1-18. https://doi.org/10.1080/15376494.2023.2206208

Jangid, R.S. (2022), "Optimum parameters and performance of tuned mass damper-inerter for base-isolated structures", *Smart Struct. Syst.*, *Int. J.*, **29**(4), 549-560. https://doi.org/10.12989/sss.2022.29.4.549

Ju, M., Dou, Z., Li, J.W., Qiu, X., Shen, B., Zhang, D., Yao, F.Z., Gong, W. and Wang, K. (2023), "Piezoelectric materials and sensors for structural health monitoring: fundamental aspects, current status, and future perspectives", *Sensors*, **23**, 543. https://doi.org/10.3390/s23010543

Khan, S. (2022), "Barriers of big data analytics for smart cities development: a context of emerging economies", *Int. J. Manag. Sci. Eng. Manag.*, **17**, 123-131. https://doi.org/10.1080/17509653.2021.1997662

Krishankumar, R. and Ecer, F. (2023), "Selection of IoT service provider for sustainable transport using q-rung orthopair fuzzy CRADIS and unknown weights", *Appl. Soft Comput.*, **132**, 109870. https://doi.org/10.1016/j.asoc.2022.109870

Lee, Y.Y., Zhao, X. and Liew, K.M. (2009), "Thermoelastic analysis of functionally graded plates using the element-free kp-Ritz method", *Smart Mater. Struct.*, **18**, 035007. https://doi.org/10.1088/0964-1726/18/3/035007

Liu, B., Yang, H. and Karekal, S. (2020), "Effect of water content on argillization of mudstone during the tunnelling process", *Rock Mech. Rock Eng.*, **53**, 799-813. https://doi.org/10.1007/s00603-019-01947-w

Liu, J., Mohammadi, M., Zhan, Y., Zheng, P., Rashidi, M. and Mehrabi, P. (2021), "Utilizing artificial intelligence to predict the superplasticizer demand of self-consolidating concrete incorporating pumice, slag, and fly ash powders", *Mater.*, **14**, 6792. https://doi.org/10.3390/ma14226792

Luo, G., He, K., Wang, Y., Zhou, W., Chen, K., Zhao, L., Xu, T., Li, Z., Li, M., Yang, P. and Wang, K. (2023), "Small blind-area, high-accuracy ultrasonic rangefinder using a broadband multi-frequency piezoelectric micromachined ultrasonic transducer array", *Measur. Sci. Technol.*, **34**, 125140. https://doi.org/10.1088/1361-6501/acf682

Mao, J.J. and Zhang, W. (2018), "Linear and nonlinear free and forced vibrations of graphene reinforced piezoelectric composite plate under external voltage excitation", *Compos. Struct.*, **203**, 551-565. https://doi.org/10.1016/j.compstruct.2018.06.076

Mehrabi, P., Honarbari, S., Rafiei, S., Jahandari, S. and Alizadeh Bidgoli, M. (2021a), "Seismic response prediction of FRC rectangular columns using intelligent fuzzy-based hybrid metaheuristic techniques", *J. Ambient Intell. Humaniz. Comput.*, **12**, 10105-10123. https://doi.org/10.1007/s12652-020-02776-4

Mehrabi, P., Shariati, M., Kabirifar, K., Jarrah, M., Rasekh, H., Trung, N.T., Shariati, A. and Jahandari, S. (2021b), "Effect of pumice powder and nano-clay on the strength and permeability of fiber-reinforced pervious concrete incorporating recycled concrete aggregate", *Constr. Build. Mater.*, **287**, 122652. https://doi.org/10.1016/j.conbuildmat.2021.122652

Mi, C., Liu, Y., Zhang, Y., Wang, J., Feng, Y. and Zhang, Z. (2023), "A vision-based displacement measurement system for foundation pit", *IEEE Transact. Instrument. Measur.*, **72**. https://doi.org/10.1109/TIM.2023.3311069

Mishra, M., Lourenço, P.B. and Ramana, G.V. (2022), "Structural health monitoring of civil engineering structures by using the internet of things: A review", *J. Build. Eng.*, **48**, 103954. https://doi.org/10.1016/j.jobe.2021.103954

Mitchell, J.A. and Reddy, J.N. (1995), "A refined hybrid plate theory for composite laminates with piezoelectric laminae", *Int. J. Solids Struct.*, **32**, 2345-2367. https://doi.org/10.1016/0020-7683(94)00229-P

Mock, M.B., Zhang, S., Pniak, B., Belt, N., Witherspoon, M. and Summers, R.M. (2021), "Substrate promiscuity of the NdmCDE N7-demethylase enzyme complex", *Biotechnol. Notes*, **2**, 18-25. https://doi.org/10.1016/j.biotno.2021.05.001

Mock, M.B., Zhang, S., Pakulski, K., Hutchison, C., Kapperman, M., Dreischarf, T. and Summers, R.M. (2024), "Production of 1-methylxanthine via the biodegradation of theophylline by an optimized Escherichia coli strain", *J. Biotechnol*., **379**, 25-32. https://doi.org/10.1016/j.jbiotec.2023.11.005

Nguyen, S.N., Cho, M., Kim, J.S. and Han, J.W. (2022), "Improved thermo-mechanical-viscoelastic analysis of laminated composite structures via the enhanced Lo–Christensen–Wu theory in the laplace domain", *Mech. Adv. Mater. Struct*., **30**(14), 2899-2915. https://doi.org/10.1080/15376494.2022.2064571

Nguyen-Xuan, H., Tran, L.V., Nguyen-Thoi, T. and Vu-Do, H.C. (2011), "Analysis of functionally graded plates using an edge-based smoothed finite element method", *Compos. Struct*., **93**, 3019-3039. https://doi.org/10.1016/j.compstruct.2011.04.028

Qiu, Y. (2019), "Estimation of tail risk measures in finance: Approaches to extreme value mixture modeling", Doctoral dissertation; Johns Hopkins University, Baltimore, MD, USA.

Qiu, Y. and Wang, J. (2024), "A Machine Learning Approach to Credit Card Customer Segmentation for Economic Stability", *Presented at the Proceedings of the 4th International Conference on Economic Management and Big Data Applications*, *ICEMBDA 2023*, Tianjin, China, October.

Quan, X. and Solheim, M.C. (2023), "Public-private partnerships in smart cities: A critical survey and research agenda", *City Culture Soc*., **32**, 100491. https://doi.org/10.1016/j.ccs.2022.100491

Rahimi, A., Alibeigloo, A. and Safarpour, M. (2020), "Three-dimensional static and free vibration analysis of graphene platelet–reinforced porous composite cylindrical shell", *J. Vib. Control*, **26**, 1627-1645. https://doi.org/10.1177/1077546320902340

Rani, S. and Kumar, R. (2022), "Bibliometric review of actuators: Key automation technology in a smart city framework", *Materials Today*: *Proceedings*., *International Conference on Latest Developments in Materials & Manufacturing*, **60**, 1800-1807. https://doi.org/10.1016/j.matpr.2021.12.469

Shafiullah, M., Rahman, S., Imteyaz, B., Aroua, M.K., Hossain, M.I. and Rahman, S.M. (2023), "Review of smart city energy modeling in Southeast Asia", *Smart Cities*., **6**, 72-99. https://doi.org/10.3390/smartcities6010005

She, A., Wang, L., Peng, Y. and Li, J. (2023), "Structural reliability analysis based on improved wolf pack algorithm AK-SS", In: *Structures*, **57**, 105289. https://doi.org/10.1016/j.istruc.2023.105289

Shetty, S., Banerjee, S., Tallur, S. and Desai, Y.M. (2023), "Real-time monitoring of residual strength in corroding steel reinforcement using ultrasonic-guided waves and multi-physics modelling", *J. Adhes. Sci. Technol*., **37**(20), 2841-2860. https://doi.org/10.1080/01694243.2022.2159292

Song, M., Kitipornchai, S. and Yang, J. (2017), "Free and forced vibrations of functionally graded polymer composite plates reinforced with graphene nanoplatelets", *Compos. Struct*., **159**, 579-588. https://doi.org/10.1016/j.compstruct.2016.09.070

Song, K., Yang, H., Liang, D., Chen, L. and Jaboyedoff, M. (2024), "Step-like displacement prediction and failure mechanism analysis of slow-moving reservoir landslide", *J. Hydrol*., **628**, 130588. https://doi.org/10.1016/j.jhydrol.2023.130588

Taheri, E., Firouzianhaji, A., Usefi, N., Mehrabi, P., Ronagh, H. and Samali, B. (2019), "Investigation of a method for strengthening perforated cold-formed steel profiles under compression loads", *Appl. Sci*., **9**, 5085. https://doi.org/10.3390/app9235085

Taheri, E., Firouzianhaji, A., Mehrabi, P., Vosough Hosseini, B. and Samali, B. (2020), "Experimental and numerical investigation of a method for strengthening cold-formed steel profiles in bending", *Appl. Sci*., **10**, 3855. https://doi.org/10.3390/app10113855

Taheri, E., Mehrabi, P., Rafiei, S. and Samali, B. (2021), "Numerical evaluation of the upright columns with partial reinforcement along with the utilisation of neural networks with combining feature-selection method to predict the load and displacement", *Appl. Sci*., **11**, 11056. https://doi.org/10.3390/app112211056

Toghroli, A., Mehrabi, P., Shariati, M., Trung, N.T., Jahandari, S. and Rasekh, H. (2020), "Evaluating the use of recycled concrete aggregate and pozzolanic additives in fiber-reinforced pervious concrete with industrial and recycled fibers", *Constr. Build. Mater*., **252**, 118997. https://doi.org/10.1016/j.conbuildmat.2020.118997

Vahidnia, M.H. (2022), "Citizen participation through volunteered geographic information as equipment for a smart city to monitor urban decay", *Environ. Monitor. Assess*., **195**, 181. https://doi.org/10.1007/s10661-022-10796-0

Wang, Q. and Liew, K.M. (2003), "Analysis of wave propagation in piezoelectric coupled cylinder affected by transverse shear and rotary inertia", *Int. J. Solids Struct*., **40**, 6653-6667. https://doi.org/10.1016/S0020-7683(03)00422-0

Wang, M. and Zhou, T. (2023), "Does smart city implementation improve the subjective quality of life? Evidence from China", *Technol. Soc*., **72**, 102161. https://doi.org/10.1016/j.techsoc.2022.102161

Wang, N., Li, X., Lian, X., Zhuang, Q., Wang, J., Li, J., Qian, H., Miao, K., Wang, Y., Luo, X. and Feng, G. (2024), "Acetate Ions Facilitated Immobilization of Highly Dispersed Transition Metal Oxide Nanoclusters in Mesoporous Silica", *Inorganic Chemistry*, **63**(9), 4393-4403. https://doi.org/10.1021/acs.inorgchem.4c00024

Wu, J., Yang, Y., Mehrabi, P. and Nasr, E.A. (2023), "Efficient machine-learning algorithm applied to predict the transient shock reaction of the elastic structure partially rested on the viscoelastic substrate", *Mech. Adv. Mater. Struct*., 1-25. https://doi.org/10.1080/15376494.2023.2183289

Xia, D., Alexander, A.K., Isbell, A., Zhang, S., Ou, J. and Liu, X.M. (2017), "Establishing a co-culture system for Clostridium cellulovorans and Clostridium aceticum for high efficiency biomass transformation", *J. Sci. Heal. Univ. Ala*., **14**, 8-13.

Yang, H., Song, K. and Zhou, J. (2022), "Automated recognition model of geomechanical information based on operational data of tunneling boring machines", *Rock Mech. Rock Eng*., **55**, 1499-1566. https://doi.org/10.1007/s00603-021-02723-5

Yang, H., Chen, C., Ni, J. and Karekal, S. (2023a), "A hyperspectral evaluation approach for quantifying salt-induced weathering of sandstone", *Sci. Total Environ*., **885**, 163886. https://doi.org/10.1016/j.scitotenv.2023.163886

Yang, H., Ni, J., Chen, C. and Chen, Y. (2023b), "Weathering assessment approach for building sandstone using hyperspectral imaging technique", *Heritage Sci*.., **11**, 70. https://doi.org/10.1186/s40494-023-00914-7

Zhang, X., Tang, Y., Zhang, F. and Lee, C.S. (2016), "A novel aluminum–graphite dual-ion battery", *Adv. Energy Mater*., **6**(11), 1502588. https://doi.org/10.1002/aenm.201502588

Zhang, J., Wang, X., Zhou, L., Liu, G., Adroja, D.T., da Silva, I., Demmel, F., Khalyavin, D., Sannigrahi, J., Nair, H.S. and Duan, L. (2022), "A ferrotoroidic candidate with well-separated spin chains", *Adv. Mater*., **34**(12), 2106728. https://doi.org/10.1002/adma.202106728

Zhong, T., Feng, X., Zhang, Y. and Zhou, J. (2022), "Experimental study on the effect of EC-TMD on the vibration control of plant structure of PSPPs", *Smart Struct. Syst*., *Int. J*., **29**(3), 457-473. https://doi.org/10.12989/sss.2022.29.3.457

Zhou, J., Qi, Q., Liu, Q., Wang, Z. and Ren, J. (2024), "Determining residual stress profile induced by end milling

from measured thin plate deformation", *Thin-Wall*. *Struct*., **200**, 111862. https://doi.org/10.1016/j.tws.2024.111862

Zhu, Q., Chen, J., Gou, G., Chen, H. and Li, P. (2017), "Ameliorated longitudinal critically refracted—Attenuation velocity method for welding residual stress measurement", *J*. *Mater*. *Process*. *Technol*., **246**, 267-275. https://doi.org/10.1016/j.jmatprotec.2017.03.022